A&A manuscript no.
(will be inserted by hand later)

Your thesaurus codes are:
intergalactic medium – quasars: absorption lines – quasars: individual: Q
0000 − 2619

ASTRONOMY
AND
ASTROPHYSICS
1.2.2008

The shape of the ionizing UV background at $z \sim 3.7$ from the metal absorption systems of Q0000 − 2619 ⋆

Sandra Savaglio[1,2], Stefano Cristiani[3], Sandro D'Odorico[1], Adriano Fontana[4], Emanuele Giallongo[4], Paolo Molaro[5]

[1] European Southern Observatory, Garching bei München, Karl-Schwarzschildstr. 2, D–85748
[2] Istituto di Astrofisica Spaziale del CNR, 00044 Frascati, Italy
[3] Dipartimento di Astronomia dell' Università, 35122 Padova, Italy
[4] Osservatorio Astronomico di Roma, Via dell' Osservatorio 2, I–00040, Monteporzio, Italy
[5] Osservatorio Astronomico di Trieste, Via G.B. Tiepolo 11, Trieste, I–34131, Italy

Received date; accepted date

Abstract.

Spectra of the $z_{em} = 4.12$ quasar Q0000 − 2619 have been obtained in the range $\lambda\lambda = 4880 - 8115$ Å with a resolution of 13 km s^{-1} and signal–to–noise ratio of $s/n = 15 - 60$ per resolution element. The list of the identified absorption lines is given together with their fitted column densities and Doppler widths. The mode of the distribution of the Doppler parameters for the Lyα lines is $\simeq 25$ km s^{-1}. The fraction of lines with $10 < b < 20$ km s^{-1} is 17%. The Doppler values derived from uncontaminated Lyβ lines are smaller than those obtained from the corresponding Lyα lines, indicating the contribution of non saturated, non resolved components in the Lyα profiles.

The integrated UV background estimated from the proximity effect is found to be $J \sim 7 \times 10^{-22}$ erg s^{-1} cm^{-2} Hz^{-1} sr^{-1}. This value is consistent with previous estimates obtained at a lower z, implying no appreciable redshift evolution of the UVB up to $z = 4$.

13 metal systems are identified, five of which previously unknown. The analysis of the associated metal systems suggests abundances generally below the solar value with an average [C/H] ~ -0.5. This value is about one order of magnitude higher than that found in intervening systems at about the same redshift.

The analysis of the intervening metal line systems has revealed in particular the presence of three optically thin systems with $\log N_{HI} \sim 15$ showing associated CIV and SiIV absorptions. In order to make the observed column densities consistent with [Si/C] ratios lower than 10 times the solar value, it is necessary to assume a large jump in the spectrum of the ionizing UV background beyond the HeII edge ($J_{912}/J_{228} \gtrsim 1000$). This result, if confirmed in other spectra at the same redshift is suggestive of a possible dominance of a stellar ionizing emissivity over the declining quasar one at $z > 3$.

Send offprint requests to: Sandro D'Odorico

⋆Based on observations collected at the European Southern Observatory, La Silla, Chile (ESO No. 2–013–49K).

Key words: Galaxies: formation of – general: intergalactic medium – quasars: Q0000 − 2619

1. Introduction

The Lyα forest detected in the blue side of the quasar Lyα emission is generally ascribed to an intergalactic population of hydrogen clouds. Lyα clouds are present at all the observed redshifts from the largest to the present epoch, (e.g. Carswell 1995; Bahcall et al. 1996; Giallongo et al. 1996), covering a substantial fraction of the total age of the universe. The origin and evolution of the clouds are intimately linked with the physical conditions and evolution of the universe (Miralda-Escudé et al. 1996). While the strongest Lyα clouds showing associated metals are thought to be associated with intervening galaxy halos (Bergeron & Boissé 1991; Bergeron et al. 1992; Steidel et al. 1994), the environment of the optically thin ones is less clear. At least at low redshift some Lyα with column densities $\gtrsim 10^{14}$ cm^{-2} have been associated with the external parts of galaxy halos (Lanzetta et al. 1995).

There are however recent observational suggestions indicating a continuity scenario between Lyα lines with $\log N_{HI} \gtrsim 14$ and the stronger metal line systems. Clustering of the Lyα clouds has been found up to scales of 300 km s^{-1}(Cristiani et al. 1995,1996; Chernomordik 1995; Hu et al. 1995; Fernandez–Soto et al. 1996) with an amplitude increasing with N_{HI}. In particular, Cristiani et al. 1996 found that an extrapolation of this trend to $\log N_{HI} \sim 17$ is consistent with the corresponding estimate derived from the CIV metal systems by Petitjean & Bergeron 1994.

Weak CIV lines have been found to be associated with Lyα lines with $\log N_{HI} = 14.5 \sim 15$ (Cowie et al. 1995; Tytler et al. 1995) with abundances similar to that of the metal line systems.

Disentangling between different scenarios for the cloud structure and their cosmological evolution requires a large database of high resolution spectra. The sample available in literature is still limited, but new impulse in the field has come

Table 1. Log of the observations.

setup	No. of spectra	date	range (Å)	FWHM (Å)	grating	CD grism	slit width	exposure (s)
E1	2	15/10/90	4700 − 6452	0.2	10	#5	1.2"	5400/6600
E2	2	18/10/90	5830 − 8550	0.3	10	#4	1.2"	4200/5100
E3	3	24-25/11/94	4820 − 8450	0.3	10	#3	1.25"/1.25"/1.3"	5000/5600/5000
G1	2	26-27/11/95	4000 − 10000	10	–	#1	5"/1.5"	900/900

from the observations with the HIRES spectrograph at the Keck telescope (Cowie et al. 1995; Hu et al. 1995)

Within an ESO Key Project on intergalactic matter at high redshift, we have obtained at the 3.5m NTT high resolution spectra of several QSOs at redshift larger than 3 (Giallongo et al. 1996). We present and discuss here in detail data on the Lyα forest and the metal systems of the QSO 0000−26 (m_R = 17.5, z_{em} = 4.12). The spectra cover the range 4880 to 8115 Å at a resolution of 13 km s^{-1}. A preliminary investigation of the spectrum of Q0000 − 26 in the range 4700 to 6600 Å at a resolution of 30 km s^{-1} has been reported by Webb et al. 1988. A first discussion of the metal systems in Q0000 − 26, based mainly on the data in the spectral region around the Lyα emission and to the red of it, has been given by Savaglio et al. 1994, while a detailed study of the metallicity of the damped Lyα system at z = 3.39 has been reported by Molaro et al. 1995.

In this paper we present in section 2 the observations, the data reduction procedure and the list of the Lyα lines and identified metal lines with the fitting parameters column density, Doppler width and redshift. The result of the statistical analysis of the Lyα forest is presented in section 3. The metal line systems are discussed in section 4.

2. Observations and data extraction

The echelle observations of Q0000 − 2619 presented here were obtained with the EMMI instrument (D'Odorico 1990) at the ESO NTT telescope in October 1990 and November 1994. The log of the observations is given in Table 1. The second column gives the number of individual spectra obtained with each setting. The seeing during the observations was typically between 0.8 and 1.2 arcsec.

The absolute flux calibration was carried out by observing of the standard stars Feige 110 (Stone 1977), LTT7987 (Stone and Baldwin 1983 and Stone and Baldwin 1984) and HD49798 (Walsh 1992).

The echelle data were reduced with the ECHELLE software package available in the MIDAS software. The wavelength calibration spectra of the Thorium-Argon lamp were extracted in the same way and used to establish the wavelength scale. Wavelengths have been corrected to vacuum heliocentric values. The weighted mean of the spectra has been obtained at the resolution of about R = 24000. The variance spectrum was obtained by propagation of the photon statistics of the object and sky spectra, and from the detector read–out–noise. The final signal–to–noise ratio per resolution element is shown in Fig. 1.

Fig. 1. Signal–to–noise ratio per resolution element as function of wavelength in the spectrum of Q0000 − 26.

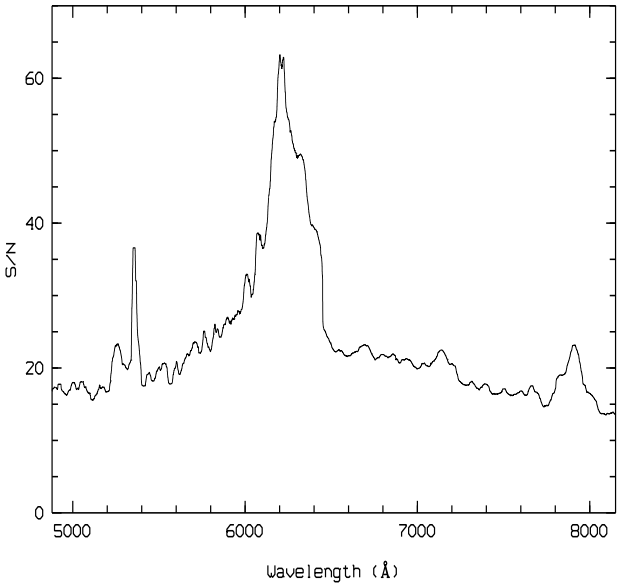

The normalized spectrum is plotted in Fig. 2 in the wavelength interval $\lambda\lambda$ = 4880 − 8115 Å. The dedicated software FITLYMAN (Fontana & Ballester 1995) in the MIDAS package was used to derive the redshift z, the Doppler parameter $b = \sqrt{2}\sigma$ and the column density N of the absorption lines. The line fitting has been performed by a χ^2 minimization of Voigt profiles, after deconvolution with the instrumental profile.

Despite the high resolution, most of the features appears to be strongly blended, contrary to what is found in lower z QSOs, where the lines are typically isolated. As in previous similar analyses (e.g. Giallongo et al. 1993), complex structures have been fitted with the minimum number of components required to give a probability of random deviation $P > 0.05$.

We performed the fitting of all the line complexes in the region with $s/n \gtrsim 20$, i.e. from z = 3.602, to the quasar Lyα emission line ($\lambda\lambda$ = 5590 − 6240 Å).

The parameter list for about 300 Lyα lines is reported in Table 2, while Table 3 lists the metal lines. Only the fitted lines appear in the tables.

Fig. 2. Absorption lines of Q0000 − 26. The normalized spectrum is shown as full line, the fit as thin line and the noise per pixel as dashed line. Long ticks correspond to Lyα and Lyβ lines, short ticks correspond to metal lines. For $\lambda < 5260$ Å the Lyβ lines are indicated with the same number as the corresponding Lyα lines.

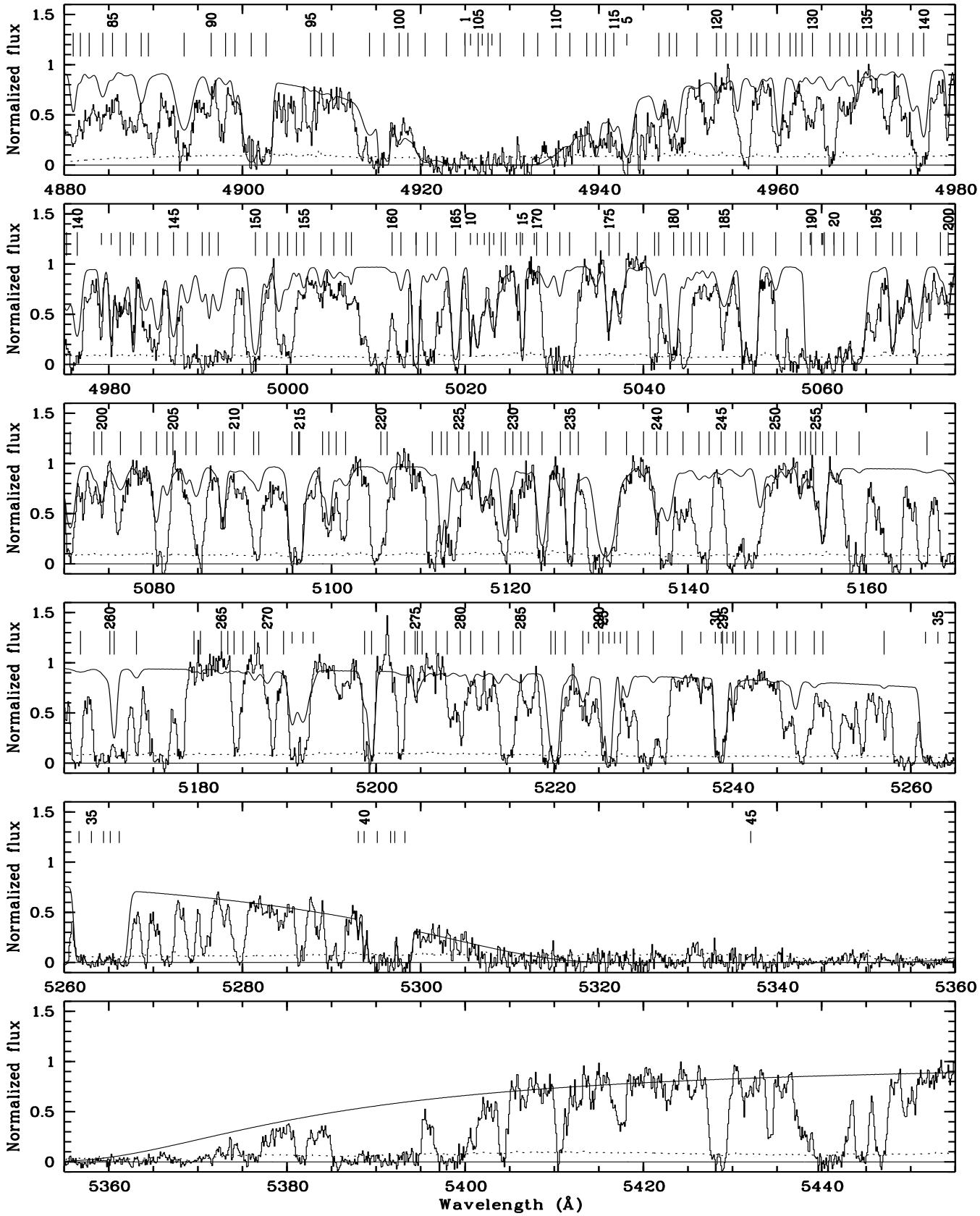

Fig. 2. – *Continued*

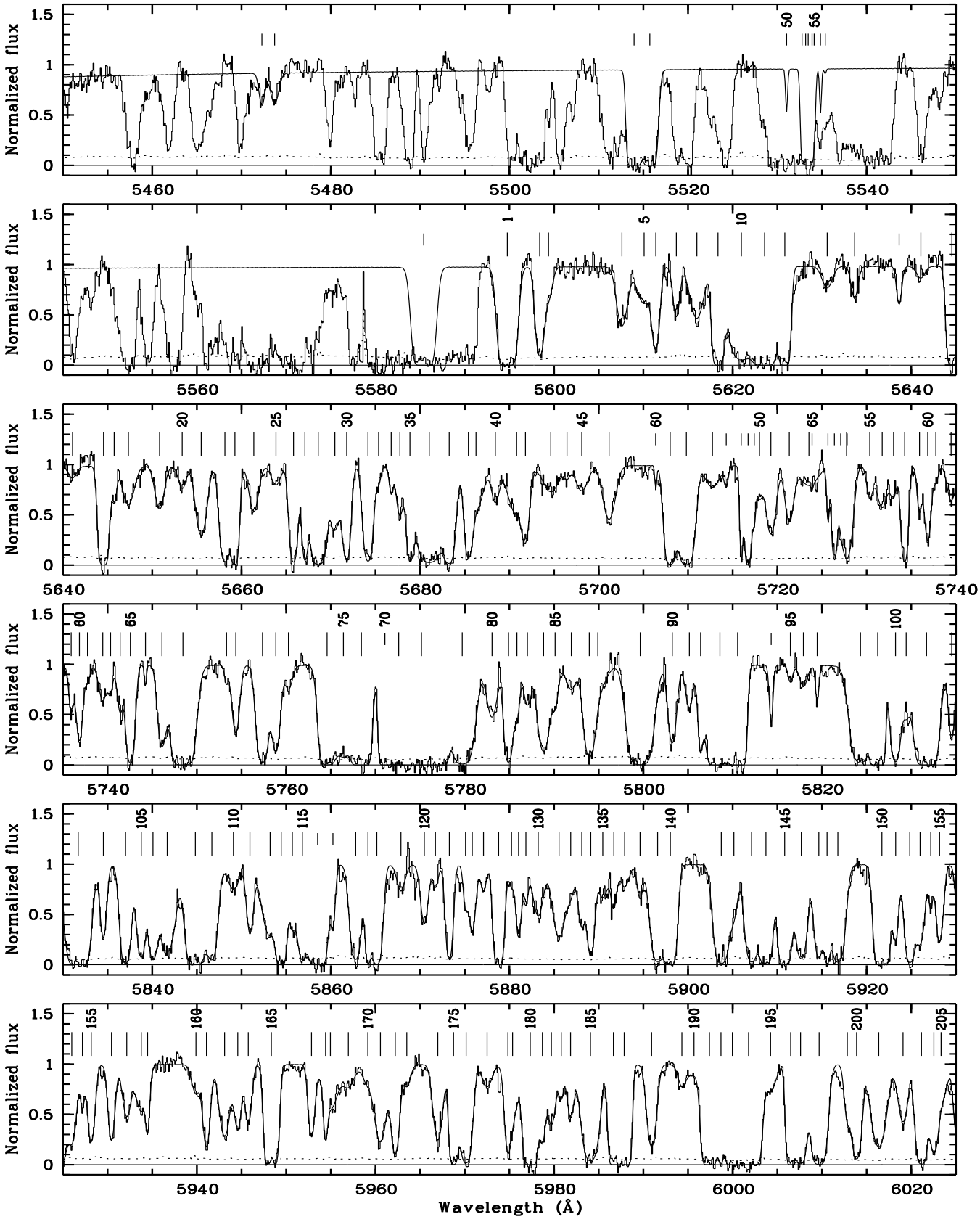

Fig. 2. – *Continued*

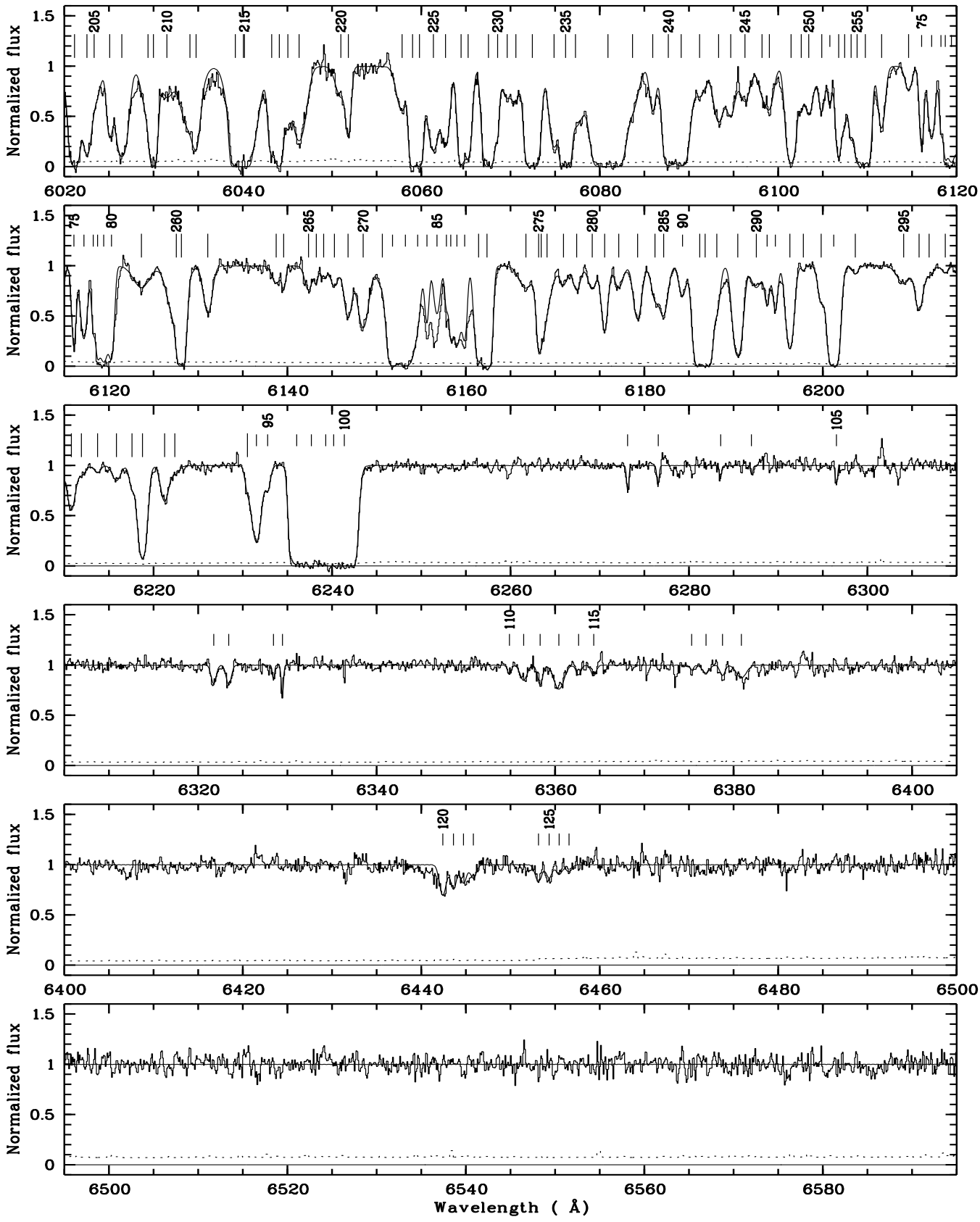

Fig. 2. – *Continued*

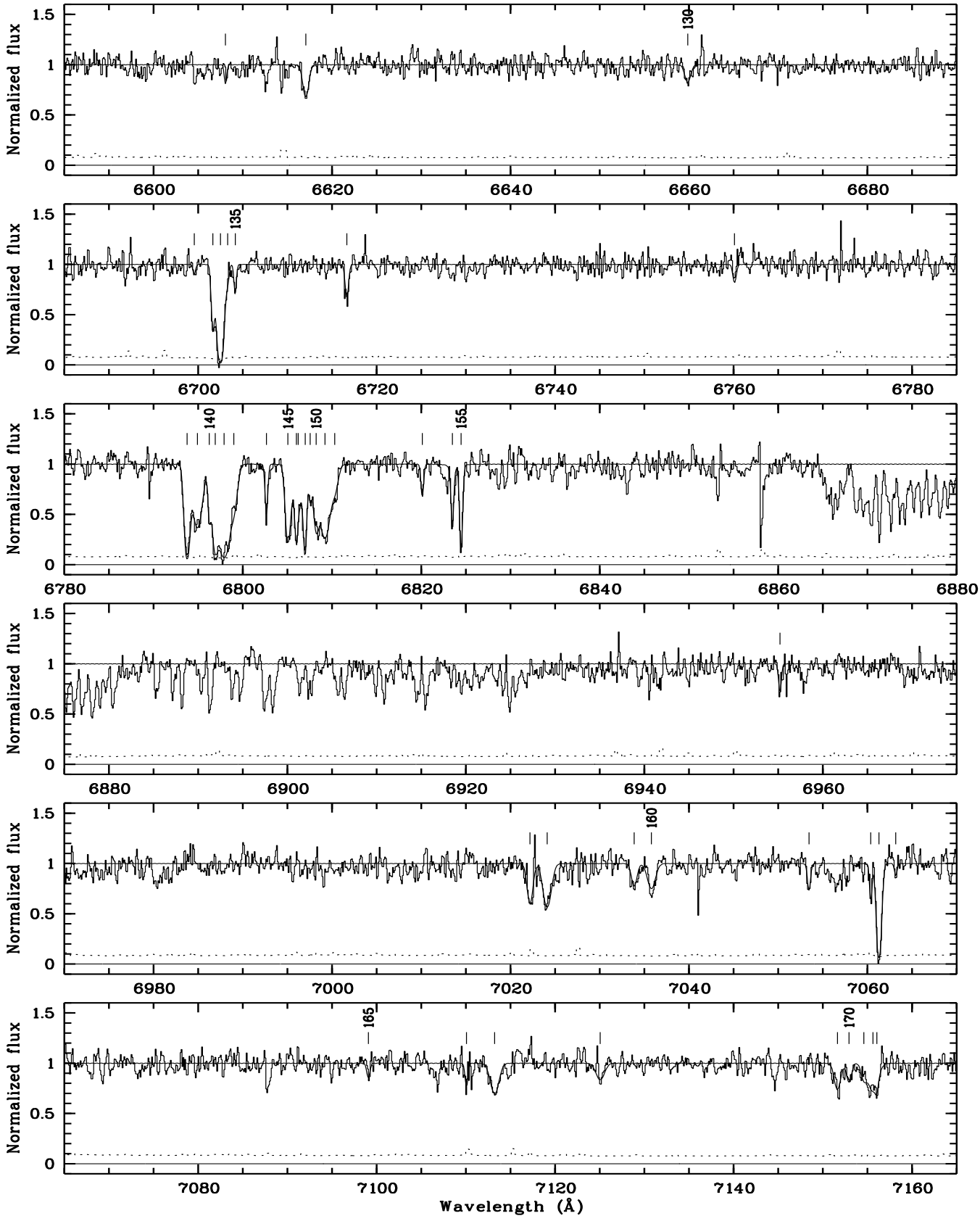

Fig. 2. – *Continued*

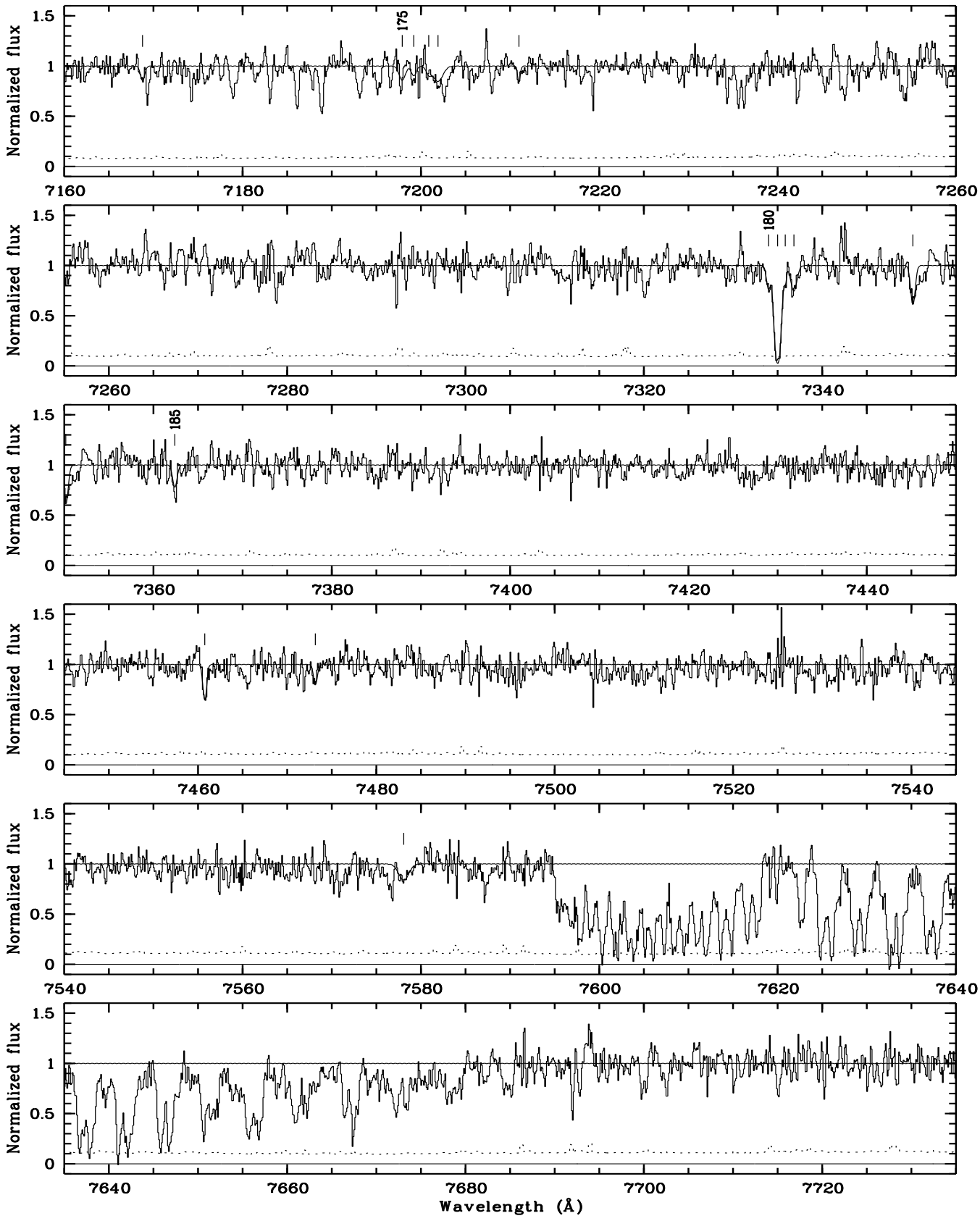

Fig. 2. – *Continued*

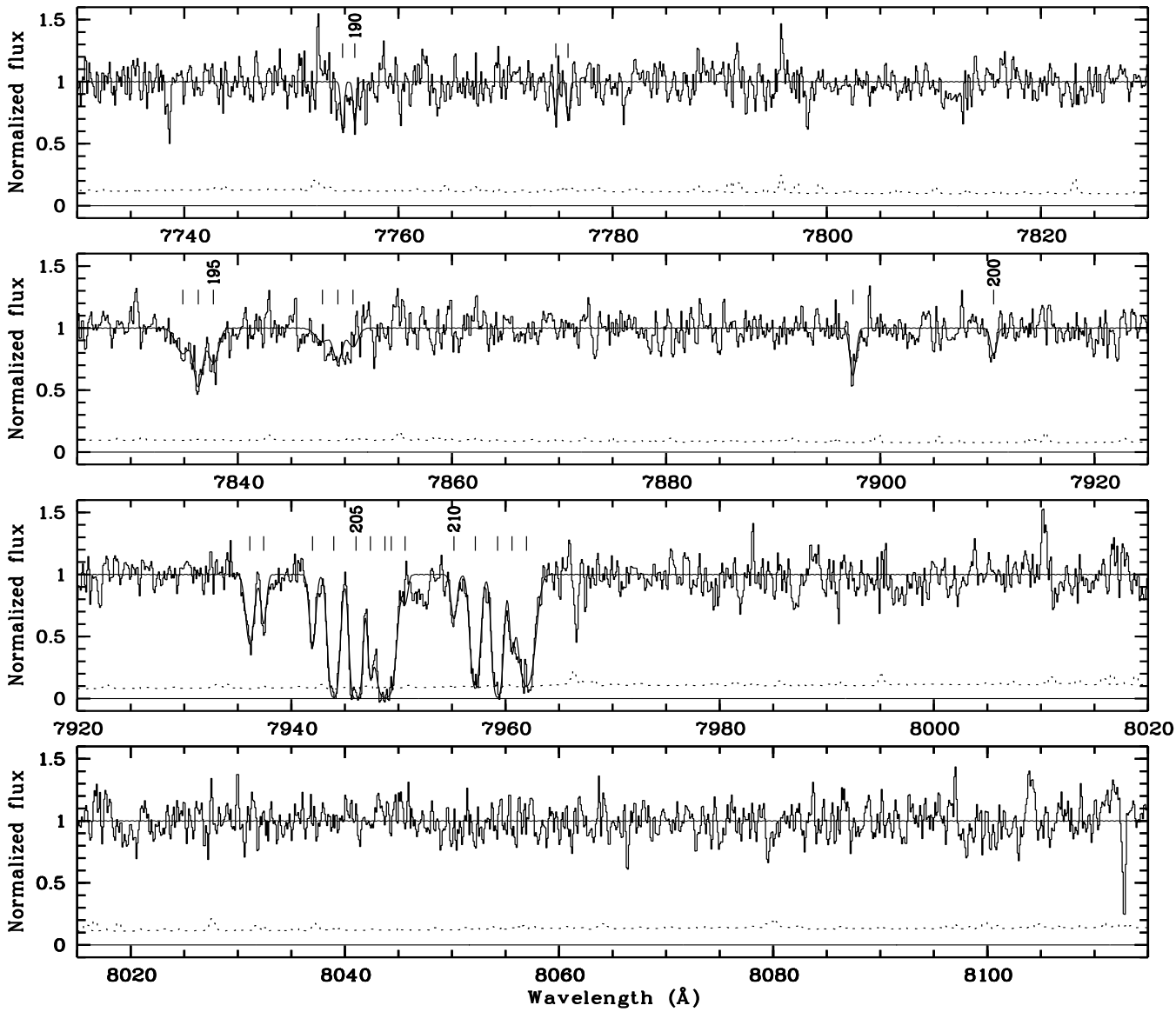

The position of fitted lines is marked on the top of Fig. 2 with the numbering as given in Table 2 and 3. Long ticks show Lyα lines (Table 2) and with the same numbering the associated Lyβ lines in the wavelength range $4880 - 5260$ Å. Short ticks are metal absorption lines (Table 3).

The Lyα forest is contaminated by the metal lines of two damped Lyα systems and other 11 metal systems, 4 of which with $z_{abs} \approx z_{em}$. In Table 3 the Lyα lines associated with metal systems are indicated as "MLyα" and taken off from the sample used for Lyα analysis and statistics.

A low resolution ($R = 280$) spectrum of $Q0000 - 26$, covering the range $\lambda\lambda = 4000 - 10000$ Å, has been obtained in the long slit mode of EMMI at the NTT in November 1995 (see Table 1). The absolute flux calibration was carried out observing the standard star Feige 110.

3. The Lyα forest

Clues on the physical nature of Lyα clouds may be obtained from the statistical distributions of their parameters (redshift, Doppler width and column density) obtained through line profile fitting.

The present data, covering a wide redshift range with good signal–to–noise, are especially suited to address the issue of the Doppler parameter distribution and to study the UV background at $z \sim 3.5 - 3.8$. The redshift evolution and column density distribution of the Lyα clouds have been already discussed using a larger data base in Giallongo et al. (1996).

3.1. The Doppler parameter distribution

While it is generally agreed that "typical" Lyα clouds have Doppler parameters of the order of $b \sim 25$ km s^{-1}, the actual fraction of narrow ($b < 20$ km s^{-1}) and broad ($b > 50$ km s^{-1}) lines is more difficult to determine, because of the possible systematic effects involved.

Large b values may be a result of the intrinsic difficulty in finding out sub-components in blends, while noise effects and the contamination of unrecognized metal lines may increase the fraction of narrow lines (Rauch et al. 1993).

The strong biases in the detection and measure of the narrow lines can be minimized with high quality data on an extended redshift range, as in the present spectrum. As shown in Fig. 3, low b values are not correlated with the wavelength and consequently with the s/n (see also Fig. 1).

The Doppler parameter distribution has been obtained by selecting all the lines out of 8 Mpc from the QSO, not affected by the proximity effect, and is shown in Fig. 4.

As usual, the distribution appears skewed towards large b values. The mode of the distribution is 25 km s^{-1} and 17% of the lines have $10 < b < 20$.

To estimate the intrinsic dispersion of the distribution we calculate iteratively the mean b value excluding lines with 2σ beyond the mean. In this way we avoid large, possible spurious b deriving a mean value $\langle b \rangle = 26$ km s^{-1} and $\sigma_b = 8$ km s^{-1}. The distribution of measurement errors has a median value $\simeq 3$ km s^{-1} so does not affect appreciably the observed b dispersion. After subtraction in quadrature we obtain $\sigma_b = 7$ km s^{-1}.

Of course any intrinsic b distribution with an artificial cut-off at the low end produces a low$-b$ tail due to measurement errors (Hu et al. 1995). A very large statistics with low measurement errors is needed to deconvolve the intrinsic distribution from the observed one. Without a very large Lyα sample, the problem of the intrinsic fraction of narrow lines remains an open question although photoionization models (Giallongo & Petitjean 1994; Ferrara & Giallongo 1996) and recent cosmological models for the Lyα clouds (Hernquist et al. 1996; Miralda–Escudé et al. 1996) are able to produce b values as low as $b \sim 15$ km s^{-1}.

3.2. The Lyβ forest and the b values

The line parameters derived from Lyα fitting have been compared with the corresponding Lyβ lines. In general the Lyβ forest is mixed with the Lyα forest at lower z, but in several cases we found isolated absorptions in correspondence of the position of the expected Lyβ. For these systems we tried a simultaneous fit for the Lyα and Lyβ components of the same cloud. Since the Lyβ line in these cases is less saturated than the corresponding Lyα, a more accurate estimate of N_{HI} and b is obtained. In Fig. 5 we show a sub-sample for which the Lyα+Lyβ fit gives a significantly different result from the fit with only the Lyα component. In general the high column density Lyα lines tend to split in more components: the initial 13 lines become 22 after decomposition. These 22 lines are marked with an asterisk in Table 2. Besides the b mean value goes from 43 km s^{-1} to 28 km s^{-1} in better agreement with the b distributions derived in Sect 3.1 and by Hu et al. (1995).

While a firm statistical conclusion cannot be drawn with these few cases, they suggest that at least some of the lines with large b are due to blends of several components. In this

Table 3. – *Continued*

#	λ_{vac}(Å)	log N	b	z	ID
153	6820.11	12.50±0.08	4.5± 1.5	1.43268	MgII-2803
154	6823.48	15.36±0.75	1.1± 5.7	1.43388	MgII-2803
155	6824.46	14.93±0.40	3.0± 0.4	1.43423	MgII-2803
156	6955.19	11.86±0.11	4.7± 8.6	3.16282	AlII-1670
157	7022.18	13.32±0.05	16.5± 3.2	3.53572	CIV-1548
158	7024.10	13.53±0.03	24.7± 2.5	3.53696	CIV-1548
159	7033.86	13.32±0.05	16.5± 3.2	3.53572	CIV-1550
160	7035.79	13.53±0.03	24.7± 2.5	3.53696	CIV-1550
161	7053.44	12.49±0.09	6.9± 3.7	4.06074	SiIV-1393
162	7060.37	13.51±0.13	3.1± 1.3	3.38954	FeII-1608
163	7061.29	14.48±0.08	11.4± 1.0	3.39011	FeII-1608
164	7063.17	12.90±0.20	3.1± 2.0	3.39128	FeII-1608
165	7099.07	12.49±0.09	6.9± 3.7	4.06074	SiIV-1402
166	7110.06	12.39±0.15	5.3± 3.5	4.10137	SiIV-1393
167	7113.22	13.35±0.05	25.9± 3.5	3.59452	CIV-1548
168	7125.05	13.35±0.05	25.9± 3.5	3.59452	CIV-1550
169	7151.63	12.75±0.07	18.5± 5.3	4.13119	SiIV-1393
170	7152.93	12.49±0.10	13.9± 6.2	4.13212	SiIV-1393
171	7154.58	12.40±0.00	15.0± 0.0	4.13331	SiIV-1393
172	7155.62	12.98±0.06	30.0± 4.6	4.13405	SiIV-1393
173	7156.05	12.39±0.15	5.3± 3.5	4.10137	SiIV-1402
174	7168.77	13.07±0.22	11.6± 9.1	3.59357	CI-1560
175	7197.89	12.75±0.07	18.5± 5.3	4.13119	SiIV-1402
176	7199.19	12.49±0.10	13.9± 6.2	4.13212	SiIV-1402
177	7200.86	12.40±0.00	15.0± 0.0	4.13331	SiIV-1402
178	7201.90	12.98±0.06	30.0± 4.6	4.13405	SiIV-1402
179	7210.98	12.27±0.16	3.8± 5.5	1.77326	FeII-2600
180	7333.99	11.89±0.14	10.5± 6.1	3.38953	AlII-1670
181	7335.00	13.15±0.14	13.7± 2.1	3.39014	AlII-1670
182	7335.85	11.60±0.25	2.5± 3.3	3.39065	AlII-1670
183	7336.81	12.09±0.10	17.3± 6.4	3.39123	AlII-1670
184	7350.17	13.20±0.12	11.5± 3.3	3.74757	CIV-1548
185	7362.39	13.20±0.12	11.5± 3.3	3.74757	CIV-1550
186	7460.75	13.08±0.08	8.6± 3.2	3.81899	CIV-1548
187	7473.16	13.08±0.08	8.6± 3.2	3.81899	CIV-1550
188	7578.06	12.07±0.12	29.7± 9.8	3.53562	AlII-1670
189	7754.78	12.43±0.25	2.4± 2.5	1.77317	MgII-2796
190	7755.92	13.50±1.79	1.6± 0.7	1.77358	MgII-2796
191	7774.69	12.43±0.25	2.4± 2.5	1.77317	MgII-2803
192	7775.83	13.50±1.79	1.6± 0.7	1.77358	MgII-2803
193	7834.86	13.24±0.16	32.4±15.4	4.06064	CIV-1548
194	7836.30	13.47±0.09	19.3± 4.2	4.06157	CIV-1548
195	7837.71	13.26±0.09	23.1± 6.7	4.06248	CIV-1548
196	7847.90	13.24±0.16	32.4±15.4	4.06064	CIV-1550
197	7849.34	13.47±0.09	19.3± 4.2	4.06157	CIV-1550
198	7850.75	13.26±0.09	23.1± 6.7	4.06248	CIV-1550
199	7897.44	13.21±0.04	12.5± 2.0	4.10106	CIV-1548
200	7910.58	13.21±0.04	12.5± 2.0	4.10106	CIV-1550
201	7936.12	13.54±0.03	16.7± 1.7	4.12604	CIV-1548
202	7937.41	13.17±0.05	10.0± 2.2	4.12688	CIV-1548
203	7941.97	13.46±0.04	11.8± 1.7	4.12982	CIV-1548
204	7943.96	14.34±0.05	16.7± 0.8	4.13110	CIV-1548
205	7946.04	14.62±0.13	15.7± 1.3	4.13245	CIV-1548
206	7947.37	13.68±0.07	8.1± 2.1	4.13331	CIV-1548
207	7948.74	14.51±0.03	29.8± 1.6	4.13419	CIV-1548
208	7949.32	13.54±0.03	16.7± 1.7	4.12604	CIV-1550
209	7950.62	13.17±0.05	10.0± 2.2	4.12688	CIV-1550
210	7955.18	13.46±0.04	11.8± 1.7	4.12982	CIV-1550
211	7957.17	14.34±0.05	16.7± 0.8	4.13110	CIV-1550
212	7959.26	14.62±0.13	15.7± 1.3	4.13245	CIV-1550
213	7960.59	13.68±0.07	8.1± 2.1	4.13331	CIV-1550
214	7961.96	14.51±0.03	29.8± 1.6	4.13419	CIV-1550

Table 2. Absorption line parameters of the Lyα forest. Lines marked with an asterisk have been fitted using simultaneously the observed Lyα and Lyβ profile.

#	λ_{vac}(Å)	$\log N$	b	z	ID
1	5594.76	14.79±0.07	41.4± 1.7	3.60220	Lyα
2	5598.39	13.95±0.05	27.2± 2.7	3.60518	Lyα
3	5599.38	13.18±0.26	29.0±11.5	3.60600	Lyα
4	5607.60	13.68±0.03	38.6± 2.5	3.61276	Lyα
5	5610.08	13.54±0.10	55.7±12.9	3.61480	Lyα
6	5611.38	13.78±0.05	24.8± 2.3	3.61587	Lyα
7	5613.68	13.38±0.05	24.5± 2.5	3.61776	Lyα
8	5615.98	13.69±0.03	49.3± 4.1	3.61965	Lyα
9	5618.35	14.56±0.43	25.6± 7.9	3.62160	Lyα
10	5620.96	14.49±0.15	79.9±27.4	3.62375	Lyα
11	5623.57	14.85±0.17	57.0±13.2	3.62590	Lyα
12	5625.83	14.66±0.23	23.6± 3.3	3.62776	Lyα
13	5630.58	13.12±0.07	39.8± 8.0	3.63166	Lyα
14	5633.65	13.13±0.06	25.5± 4.3	3.63419	Lyα
15	5641.06	12.75±0.12	32.6± 9.2	3.64028	Lyα
16	5644.54	14.44±0.13	24.4± 2.5	3.64315	Lyα
17	5645.73	13.05±0.12	17.7± 5.5	3.64413	Lyα
18	5647.32	13.46±0.03	43.9± 4.4	3.64543	Lyα
19	5650.81	13.43±0.03	34.6± 3.0	3.64831	Lyα
20	5653.35	13.02±0.07	30.0± 6.4	3.65039	Lyα
21	5655.48	13.79±0.02	38.2± 1.8	3.65215	Lyα
22	5658.13	14.14±0.05	29.9± 2.9	3.65433	Lyα
23	5659.25	14.21±0.11	21.1± 2.2	3.65525	Lyα
24	5661.37	13.46±0.03	34.5± 3.2	3.65699	Lyα
25	5663.85	13.02±0.07	36.5± 7.2	3.65903	Lyα
26	5665.81	14.07±0.04	23.7± 1.5	3.66064	Lyα
27	5667.09	13.89±0.07	18.2± 2.6	3.66170	Lyα
28	5668.59	14.46±0.10	39.8± 7.5	3.66293	Lyα
29	5670.44	13.73±0.13	38.4±12.9	3.66445	Lyα
30	5671.77	14.00±0.05	23.9± 2.0	3.66555	Lyα
31	5674.16	14.11±0.05	28.7± 1.9	3.66751	Lyα
32	5675.35	12.66±0.17	16.5± 8.3	3.66849	Lyα
33	5676.75	12.84±0.12	14.5± 5.2	3.66964	Lyα
34	5677.73	13.38±0.05	25.6± 4.1	3.67045	Lyα
35	5678.86	13.93±0.11	19.6± 3.0	3.67138	Lyα
36	5681.02	14.57±0.04	75.8±15.5	3.67316	Lyα
37	5683.25	14.23±0.09	33.2± 4.2	3.67499	Lyα
38	5685.39	13.91±0.04	25.0± 1.9	3.67675	Lyα
39	5686.25	13.61±0.04	53.3± 6.7	3.67746	Lyα
40	5688.42	13.25±0.05	29.1± 4.0	3.67924	Lyα
41	5690.79	13.75±0.10	63.5±10.0	3.68119	Lyα
42	5691.78	13.61±0.12	25.0± 4.3	3.68201	Lyα
43	5694.63	13.39±0.05	60.6± 8.9	3.68435	Lyα
44	5696.43	12.58±0.25	23.1±13.1	3.68583	Lyα
45	5698.10	13.26±0.05	46.7± 7.3	3.68721	Lyα
46	5701.15	13.67±0.02	44.9± 2.6	3.68971	Lyα
47	5707.99	14.32±0.07	30.7± 2.6	3.69534	Lyα
48	5709.80	14.47±0.05	41.4± 2.7	3.69683	Lyα
49	5712.73	13.25±0.05	54.0± 7.1	3.69924	Lyα
50	5718.00	13.05±0.06	21.1± 4.1	3.70358	Lyα
51	5719.28	13.74±0.02	34.8± 1.9	3.70463	Lyα
52	5721.34	13.54±0.03	30.8± 2.4	3.70632	Lyα
53	5723.54	13.32±0.07	70.6±14.7	3.70813	Lyα
54	5727.75	14.10±0.03	36.3± 1.9	3.71159	Lyα
55	5730.34	13.07±0.08	21.8± 4.3	3.71373	Lyα
56	5731.73	13.47±0.06	40.0± 7.1	3.71487	Lyα
57	5733.01	13.09±0.06	24.1± 4.0	3.71592	Lyα
58	5734.25	14.00±0.06	19.6± 1.4	3.71694	Lyα
59	5735.92	13.18±0.08	16.4± 4.6	3.71832	Lyα
60	5736.84	13.63±0.04	21.3± 2.6	3.71907	Lyα
61	5737.75	12.68±0.12	17.3± 7.3	3.71982	Lyα
62	5739.46	13.25±0.11	30.0± 8.3	3.72123	Lyα
63	5740.32	12.87±0.27	16.7± 8.6	3.72193	Lyα
64	5741.41	13.28±0.06	21.3± 4.2	3.72283	Lyα
65	5742.55	14.13±0.06	23.5± 1.7	3.72377	Lyα
66	5744.24	12.53±1.11	2.5± 6.4	3.72516	Lyα
67	5746.08	13.79±0.03	27.3± 2.0	3.72667	Lyα
68	5748.43	14.78±0.07	54.4± 3.0	3.72861	Lyα
69	5753.31	12.61±0.18	13.8± 9.0	3.73262	Lyα
70	5754.35	13.60±0.03	25.2± 2.2	3.73348	Lyα
71	5757.34	14.22±0.04	32.8± 2.0	3.73594	Lyα
72	5758.84	13.86±0.03	26.6± 2.5	3.73717	Lyα
73	5760.25	13.03±0.09	28.8± 8.1	3.73833	Lyα
74	5764.58	14.57±0.19	38.4± 6.6	3.74189	Lyα
75	5766.40	14.30±0.09	59.7±17.0	3.74339	Lyα
76	5768.41	15.09±0.17	36.6± 4.4	3.74504	Lyα
77	5772.59	14.61±1.27	53.6±50.0	3.74848	Lyα *
78	5775.14	17.54±0.58	56.3± 5.4	3.75058	Lyα *
79	5779.71	14.57±0.04	60.2± 3.1	3.75434	Lyα
80	5783.04	13.56±0.03	36.8± 3.0	3.75708	Lyα
81	5784.89	14.09±0.05	24.5± 2.3	3.75860	Lyα
82	5785.84	13.28±0.14	17.3± 4.9	3.75938	Lyα
83	5787.01	13.31±0.06	29.5± 5.2	3.76034	Lyα
84	5788.82	14.00±0.03	36.9± 3.5	3.76183	Lyα
85	5790.11	13.21±0.14	22.8± 7.4	3.76289	Lyα
86	5791.92	13.18±0.07	40.3± 7.9	3.76438	Lyα
87	5793.94	14.04±0.08	34.0± 3.4	3.76604	Lyα
88	5794.89	13.38±0.33	57.4±19.3	3.76682	Lyα
89	5799.64	14.68±0.06	60.4±3.4	3.77073	Lyα
90	5803.23	13.76±0.03	27.6±1.7	3.77368	Lyα
91	5805.14	13.33±0.05	28.0±4.5	3.77526	Lyα
92	5806.40	13.64±0.06	16.2±2.2	3.77629	Lyα
93	5808.56	15.15±0.06	50.3±5.1	3.77807	Lyα *
94	5810.54	15.64±0.22	25.9±2.1	3.77970	Lyα *
95	5816.46	12.64±0.10	16.2±4.9	3.78457	Lyα
96	5817.92	12.99±0.07	30.0±5.9	3.78577	Lyα
97	5819.46	12.90±0.06	10.8±3.3	3.78703	Lyα
98	5824.30	14.44±0.04	54.2±3.4	3.79102	Lyα
99	5826.23	17.29±0.53	15.5±1.5	3.79260	Lyα
100	5828.23	14.11±0.04	27.8±2.7	3.79425	Lyα
101	5829.42	13.42±0.04	28.5±3.4	3.79523	Lyα
102	5831.70	14.84±0.08	51.1±2.6	3.79710	Lyα
103	5834.52	13.59±0.02	21.0±1.3	3.79942	Lyα
104	5837.00	14.22±0.05	28.8±1.6	3.80146	Lyα
105	5838.76	13.98±0.03	26.8±2.4	3.80291	Lyα
106	5840.07	14.00±0.05	25.1±3.2	3.80399	Lyα
107	5841.67	14.13±0.03	49.5±4.9	3.80530	Lyα
108	5844.82	14.65±0.09	44.6±4.9	3.80790	Lyα
109	5846.67	14.11±0.06	32.4±3.0	3.80942	Lyα
110	5849.09	13.21±0.06	43.3±8.4	3.81141	Lyα
111	5850.94	13.56±0.03	22.7±1.6	3.81293	Lyα
112	5853.19	13.95±0.09	53.9±8.5	3.81478	Lyα
113	5854.44	14.51±0.37	22.5±7.2	3.81581	Lyα
114	5855.68	13.53±0.30	24.2±16.2	3.81683	Lyα
115	5856.80	14.05±0.16	27.6±12.1	3.81775	Lyα
116	5862.77	14.11±0.03	32.1±2.1	3.82266	Lyα
117	5864.16	13.98±0.14	14.5±3.2	3.82380	Lyα
118	5865.14	14.30±0.07	27.5±3.3	3.82461	Lyα
119	5867.85	13.09±0.06	29.6±5.4	3.82684	Lyα
120	5870.46	13.50±0.03	25.7±2.7	3.82899	Lyα
121	5871.70	12.87±0.17	20.3±11.2	3.83001	Lyα
122	5873.26	13.94±0.04	21.0±1.0	3.83129	Lyα
123	5875.07	13.06±0.16	14.6±6.0	3.83278	Lyα
124	5875.83	13.55±0.05	22.9±3.2	3.83340	Lyα
125	5877.09	12.94±0.07	20.0±4.2	3.83444	Lyα
126	5878.79	14.38±0.08	24.6±1.5	3.83584	Lyα
127	5880.23	12.81±0.08	18.2±3.8	3.83702	Lyα
128	5881.02	13.52±0.03	17.9±1.3	3.83767	Lyα
129	5881.83	13.06±0.09	15.9±5.1	3.83834	Lyα
130	5883.21	13.55±0.02	36.7±2.4	3.83947	Lyα
131	5885.55	13.86±0.03	42.1±3.7	3.84140	Lyα
132	5886.85	13.09±0.18	27.5±8.7	3.84247	Lyα
133	5888.10	13.53±0.08	25.2±5.1	3.84350	Lyα
134	5889.11	13.86±0.04	21.8±2.2	3.84433	Lyα
135	5890.44	13.31±0.06	38.1±6.8	3.84542	Lyα
136	5891.68	13.19±0.06	20.5±2.9	3.84644	Lyα
137	5892.89	13.05±0.10	33.1±11.0	3.84744	Lyα
138	5894.62	13.06±0.07	19.6±4.9	3.84886	Lyα
139	5896.59	14.26±0.08	39.1±4.6	3.85048	Lyα
140	5898.02	14.47±0.13	28.8±2.5	3.85166	Lyα
141	5903.72	14.36±0.05	39.0±3.0	3.85635	Lyα
142	5905.12	13.42±0.18	28.0±7.7	3.85750	Lyα *
143	5907.11	14.24±0.05	36.1±3.5	3.85913	Lyα
144	5908.71	14.43±0.14	31.4±5.7	3.86045	Lyα
145	5910.82	14.51±0.13	30.5±4.2	3.86219	Lyα
146	5912.68	14.11±0.03	34.0±2.7	3.86372	Lyα
147	5914.64	14.01±0.06	27.8±3.7	3.86533	Lyα
148	5915.57	13.96±0.16	14.6±4.7	3.86609	Lyα
149	5916.77	14.27±0.04	37.8±2.4	3.86708	Lyα
150	5921.71	14.79±0.13	31.6±2.5	3.87114	Lyα
151	5923.25	13.58±0.05	19.1±2.8	3.87241	Lyα
152	5924.83	14.16±0.05	28.1±3.0	3.87371	Lyα

Table 2. – *Continued*

#	λ_{vac}(Å)	$\log N$	b	z	ID
153	5925.99	13.79±0.08	29.2±4.6	3.87467	Lyα
154	5927.17	13.02±0.09	12.2±3.5	3.87564	Lyα
155	5928.16	13.69±0.02	23.5±1.6	3.87645	Lyα
156	5930.43	13.64±0.02	21.8±1.3	3.87832	Lyα
157	5932.14	13.47±0.04	29.8±3.2	3.87972	Lyα
158	5933.76	13.51±0.11	38.2±9.6	3.88106	Lyα
159	5934.48	13.25±0.15	11.9±3.1	3.88165	Lyα
160	5939.89	13.15±0.05	30.1±4.8	3.88610	Lyα
161	5941.07	13.74±0.02	23.0±1.1	3.88707	Lyα
162	5943.10	13.78±0.03	35.5±3.2	3.88874	Lyα
163	5944.58	13.53±0.04	23.6±2.6	3.88996	Lyα
164	5945.75	13.45±0.03	23.0±1.9	3.89092	Lyα
165	5948.34	14.84±0.13	26.3±1.5	3.89305	Lyα
166	5952.83	13.57±0.02	20.5±1.1	3.89674	Lyα
167	5954.41	13.26±0.07	11.3±2.0	3.89804	Lyα
168	5954.94	13.61±0.04	51.3±6.0	3.89848	Lyα
169	5956.96	13.17±0.09	43.7±8.4	3.90014	Lyα
170	5959.13	13.03±0.20	35.8±11.7	3.90193	Lyα
171	5960.55	13.87±0.04	37.3±4.2	3.90309	Lyα
172	5962.20	13.88±0.02	24.4±1.8	3.90445	Lyα
173	5963.50	12.96±0.08	26.8±5.6	3.90552	Lyα
174	5966.98	13.77±0.02	30.7±1.4	3.90838	Lyα
175	5968.74	14.30±0.04	20.4±1.3	3.90983	Lyα
176	5970.14	14.24±0.03	30.9±1.6	3.91098	Lyα
177	5972.50	13.09±0.05	36.2±5.6	3.91292	Lyα
178	5974.82	13.67±0.05	19.2±1.9	3.91483	Lyα
179	5975.35	13.60±0.07	38.3±6.2	3.91527	Lyα
180	5977.33	14.88±0.24	26.9±3.8	3.91690	Lyα
181	5978.68	13.58±0.10	17.9±4.0	3.91801	Lyα
182	5979.69	13.57±0.07	29.5±5.8	3.91884	Lyα
183	5980.80	12.98±0.13	16.6±5.1	3.91975	Lyα
184	5981.84	13.39±0.04	23.6±3.1	3.92061	Lyα
185	5984.07	14.31±0.02	46.5±1.6	3.92244	Lyα
186	5986.64	14.69±0.06	19.1±1.8	3.92456	Lyα ∗
187	5987.85	15.58±0.18	20.5±1.3	3.92555	Lyα ∗
188	5990.92	13.84±0.02	29.6±1.3	3.92808	Lyα
189	5994.31	12.88±0.08	26.2±6.0	3.93086	Lyα
190	5995.66	13.04±0.23	70.4±44.3	3.93198	Lyα
191	5997.39	14.82±0.16	30.2±3.2	3.93340	Lyα ∗
192	5998.68	14.10±0.51	11.0±6.7	3.93446	Lyα ∗
193	5999.96	14.94±0.08	26.7±3.6	3.93551	Lyα ∗
194	6001.78	15.26±0.06	41.8±2.6	3.93701	Lyα ∗
195	6004.24	13.20±0.06	37.5±6.2	3.93903	Lyα
196	6006.48	14.57±0.05	18.1±1.0	3.94088	Lyα ∗
197	6007.59	14.30±0.04	30.6±3.4	3.94179	Lyα ∗
198	6009.67	14.49±0.06	36.6±2.2	3.94350	Lyα
199	6012.83	13.34±0.04	20.2±2.3	3.94610	Lyα
200	6013.87	14.05±0.02	28.5±1.6	3.94695	Lyα
201	6016.35	14.03±0.01	46.4±1.5	3.94899	Lyα
202	6019.07	13.59±0.02	33.8±2.0	3.95123	Lyα
203	6021.14	14.32±0.05	28.5±1.8	3.95294	Lyα
204	6022.53	13.83±0.21	24.3±4.4	3.95408	Lyα
205	6023.34	13.39±0.61	39.4±39.6	3.95474	Lyα
206	6025.07	13.50±0.04	19.4±1.7	3.95617	Lyα
207	6026.44	14.07±0.02	37.7±1.9	3.95729	Lyα
208	6029.37	13.57±0.23	41.1±10.3	3.95971	Lyα
209	6029.98	14.16±0.11	20.1±3.2	3.96021	Lyα
210	6031.48	13.32±0.04	44.3±4.8	3.96144	Lyα
211	6034.07	13.92±0.07	61.7±6.2	3.96357	Lyα
212	6034.75	13.53±0.15	23.5±5.4	3.96413	Lyα
213	6039.16	14.82±0.09	18.6±2.0	3.96776	Lyα ∗
214	6040.06	14.47±0.06	68.5±3.7	3.96850	Lyα ∗
215	6040.17	14.93±0.10	20.8±2.3	3.96859	Lyα ∗
216	6043.23	13.81±0.15	21.5±3.1	3.97111	Lyα
217	6044.08	14.21±0.04	19.9±1.6	3.97181	Lyα
218	6045.04	13.29±0.04	17.4±2.3	3.97260	Lyα
219	6046.30	13.91±0.06	44.7±7.7	3.97363	Lyα
220	6050.99	13.28±0.15	39.1±12.0	3.97749	Lyα
221	6051.82	13.43±0.09	16.9±2.3	3.97817	Lyα
222	6057.84	13.49±0.05	39.4±4.7	3.98312	Lyα
223	6059.02	14.35±0.36	14.7±3.5	3.98409	Lyα
224	6059.80	14.22±0.23	18.3±5.0	3.98474	Lyα
225	6061.35	13.94±0.02	35.0±2.9	3.98601	Lyα
226	6062.71	13.75±0.03	26.3±1.7	3.98713	Lyα
227	6064.46	14.02±0.07	19.4±1.8	3.98857	Lyα
228	6065.24	13.87±0.08	22.0±2.5	3.98921	Lyα
230	6067.53	14.47±0.04	27.3±0.8	3.99109	Lyα
229	6067.53	14.47±0.04	27.3±0.8	3.99109	Lyα
230	6068.55	13.18±0.06	9.9±1.8	3.99193	Lyα
231	6069.62	13.32±0.04	41.7±4.6	3.99281	Lyα
232	6070.60	13.06±0.06	23.5±2.8	3.99362	Lyα
233	6072.44	14.66±0.01	32.3±0.2	3.99513	Lyα
234	6074.88	13.83±0.02	30.5±1.9	3.99714	Lyα
235	6076.16	15.14±0.37	18.7±2.9	3.99819	Lyα ∗
236	6077.27	13.86±0.13	59.3±15.5	3.99911	Lyα
237	6080.92	15.13±0.13	62.2±5.7	4.00211	Lyα
238	6083.66	13.47±0.14	43.4±8.2	4.00436	Lyα
239	6085.94	13.26±0.03	21.9±2.2	4.00624	Lyα
240	6087.68	14.26±0.05	28.7±2.3	4.00767	Lyα
241	6089.12	14.42±0.05	38.9±3.1	4.00885	Lyα
242	6091.19	13.34±0.07	45.6±8.5	4.01056	Lyα
243	6093.32	13.57±0.04	34.1±3.3	4.01231	Lyα
244	6094.67	13.45±0.05	30.9±3.8	4.01342	Lyα
245	6096.26	13.33±0.04	36.8±4.5	4.01473	Lyα
246	6098.18	13.04±0.49	28.9±16.9	4.01631	Lyα
247	6099.01	13.33±0.24	30.1±8.0	4.01699	Lyα
248	6101.44	14.11±0.02	28.2±1.1	4.01899	Lyα
249	6102.57	12.88±0.15	11.7±3.7	4.01992	Lyα
250	6103.42	13.45±0.05	31.2±4.5	4.02062	Lyα
251	6104.87	13.25±0.04	21.1±2.8	4.02181	Lyα
252	6106.77	13.80±0.01	18.0±0.3	4.02337	Lyα ∗
253	6107.44	13.17±0.31	12.4±18.5	4.02392	Lyα ∗
254	6108.17	13.54±0.02	18.0±1.4	4.02453	Lyα ∗
255	6108.83	13.77±0.04	12.1±0.7	4.02507	Lyα ∗
256	6109.76	14.51±0.02	24.0±0.4	4.02583	Lyα ∗
257	6111.58	13.49±0.04	22.9±2.2	4.02733	Lyα
258	6114.60	12.96±0.04	23.9±3.2	4.02981	Lyα
259	6123.64	13.28±0.03	58.9±5.3	4.03725	Lyα
260	6127.54	13.79±0.04	55.2±2.1	4.04046	Lyα
261	6128.11	14.34±0.12	19.8±1.9	4.04093	Lyα
262	6131.07	13.41±0.02	29.7±1.4	4.04336	Lyα
263	6138.73	12.89±0.08	29.8±7.1	4.04966	Lyα
264	6139.58	12.68±0.09	12.1±2.3	4.05036	Lyα
265	6142.36	13.01±0.04	26.9±3.3	4.05265	Lyα
266	6143.23	12.44±0.11	9.4±3.6	4.05337	Lyα
267	6144.05	12.60±0.10	21.3±5.9	4.05404	Lyα
268	6145.26	12.92±0.06	26.7±5.2	4.05503	Lyα
269	6146.79	13.42±0.02	26.4±1.5	4.05629	Lyα
270	6148.48	13.66±0.01	35.2±1.2	4.05768	Lyα
271	6150.63	13.06±0.09	37.8±9.6	4.05946	Lyα
272	6161.42	13.97±0.07	22.5±2.7	4.06833	Lyα
273	6162.36	14.71±0.06	19.4±1.0	4.06910	Lyα
274	6166.72	13.22±0.05	49.6±6.3	4.07269	Lyα
275	6168.14	13.26±0.20	12.3±3.1	4.07386	Lyα
276	6168.43	13.61±0.22	26.0±4.4	4.07409	Lyα
277	6169.08	13.34±0.42	38.9±14.6	4.07463	Lyα
278	6170.93	12.90±0.05	27.4±3.8	4.07615	Lyα
279	6172.41	13.00±0.03	26.4±2.8	4.07737	Lyα
280	6174.15	13.02±0.04	29.1±3.9	4.07880	Lyα
281	6175.54	13.48±0.01	20.5±0.8	4.07994	Lyα
282	6177.12	13.00±0.03	29.6±3.2	4.08124	Lyα
283	6179.23	13.45±0.01	27.3±0.9	4.08298	Lyα
284	6181.19	13.15±0.08	26.2±3.5	4.08459	Lyα
285	6182.15	13.41±0.05	28.0±2.5	4.08538	Lyα
286	6186.20	14.44±0.04	30.3±0.8	4.08871	Lyα
287	6186.80	14.87±0.08	25.6±0.9	4.08921	Lyα
288	6188.11	13.26±0.03	21.0±1.8	4.09028	Lyα
289	6190.46	13.96±0.01	28.9±0.5	4.09222	Lyα
290	6192.55	13.08±0.02	37.1±2.2	4.09394	Lyα
291	6196.30	13.78±0.01	24.8±0.5	4.09702	Lyα
292	6197.81	11.92±0.15	8.2±5.5	4.09826	Lyα
293	6199.82	13.15±0.03	22.5±1.9	4.09991	Lyα
294	6203.64	12.36±0.09	18.9±5.2	4.10306	Lyα
295	6209.05	13.08±0.04	46.9±5.0	4.10751	Lyα
296	6210.78	13.31±0.04	25.5±2.1	4.10893	Lyα
297	6211.91	12.61±0.17	29.8±11.1	4.10986	Lyα
298	6213.71	12.36±0.09	22.0±6.7	4.11134	Lyα
299	6215.84	12.82±0.04	30.0±4.1	4.11309	Lyα
300	6217.58	12.84±0.05	18.8±2.7	4.11453	Lyα
301	6218.75	13.97±0.01	25.7±0.5	4.11549	Lyα
302	6221.23	13.21±0.04	26.8±2.0	4.11753	Lyα
303	6222.38	12.57±0.19	30.5±13.7	4.11847	Lyα
304	6230.51	12.78±0.19	17.2±5.4	4.12516	Lyα

Table 3. Absorption line parameters of the metal systems.

#	λ_{vac}(Å)	log N	b	z	ID
1	4924.96	13.51±0.13	3.1± 1.3	3.38954	FeII-1121
2	4925.60	14.48±0.08	11.4± 1.0	3.39011	FeII-1121
3	4926.91	12.90±0.20	3.1± 2.0	3.39128	FeII-1121
4	4928.00	20.20±0.00	40.0± 0.0	3.05373	MLyα
5	4943.13	14.81±0.23	39.3± 8.0	3.81916	MLyβ
6	4979.16	14.69±0.04	13.9± 1.3	3.39015	NI-1134.1
7	4980.26	14.69±0.04	13.9± 1.3	3.39015	NI-1134.4
8	4982.74	14.69±0.04	13.9± 1.3	3.39015	NI-1134.9
9	5014.46	14.22±0.25	16.0± 2.2	4.13240	CIII-977
10	5020.58	12.93±0.13	8.2± 2.5	3.16127	SiIII-1206
11	5021.35	13.18±0.06	24.7± 5.5	3.16191	SiIII-1206
12	5022.13	12.55±0.24	15.9±10.1	3.16256	SiIII-1206
13	5023.20	13.00±0.03	27.8± 2.6	3.16344	SiIII-1206
14	5025.75	13.51±0.13	3.1± 1.3	3.38954	FeII-1144
15	5026.41	14.48±0.08	11.4± 1.0	3.39011	FeII-1144
16	5027.75	12.90±0.20	3.1± 2.0	3.39128	FeII-1144
17	5058.73	15.88±1.44	16.2± 5.9	3.16126	MLyα
18	5060.00	15.39±4.00	15.1± 3.2	3.16231	MLyα
19	5060.13	15.99±0.65	15.8± 4.6	3.16242	MLyα
20	5061.38	15.37±0.63	15.0± 2.5	3.16344	MLyα
21	5190.56	14.27±0.06	26.7± 3.9	4.06039	MLyβ
22	5191.78	14.48±0.07	44.1± 7.3	4.06158	MLyβ
23	5192.94	13.19±0.12	21.4± 5.6	4.06271	MLyβ
24	5223.83	12.56±0.11	4.0± 2.4	3.38823	SiII-1190
25	5225.45	13.68±0.05	6.4± 0.9	3.38960	SiII-1190
26	5226.11	14.47±0.05	16.1± 1.3	3.39015	SiII-1190
27	5226.75	12.84±0.13	6.8± 3.4	3.39069	SiII-1190
28	5227.42	13.20±0.19	2.3± 0.7	3.39125	SiII-1190
29	5236.44	12.56±0.11	4.0± 2.4	3.38823	SiII-1193
30	5238.07	13.68±0.05	6.4± 0.9	3.38960	SiII-1193
31	5238.73	14.47±0.05	16.1± 1.3	3.39015	SiII-1193
32	5239.37	12.84±0.13	6.8± 3.4	3.39069	SiII-1193
33	5240.04	13.20±0.19	2.3± 0.7	3.39125	SiII-1193
34	5261.65	15.02±0.22	24.0± 0.0	4.12970	MLyβ
35	5263.04	15.80±0.93	27.8±15.6	4.13105	MLyβ
36	5264.40	15.00±0.21	24.0± 0.0	4.13238	MLyβ
37	5265.16	14.56±0.47	25.0± 0.0	4.13312	MLyβ
38	5266.16	15.39±0.27	38.8± 3.1	4.13410	MLyβ
39	5293.00	14.41±4.67	2.1± 8.5	4.10111	OVI-1037
40	5293.65	14.48±0.93	5.8± 3.1	4.12987	OVI-1031
41	5295.12	17.00±0.28	23.3± 4.4	4.13130	OVI-1031
42	5296.62	16.18±2.83	10.6± 8.6	4.13275	OVI-1031
43	5297.08	14.25±5.81	3.2± 7.5	4.13320	OVI-1031
44	5298.23	17.00±0.02	18.0± 0.7	4.13430	OVI-1031
45	5337.04	21.30±0.00	40.0± 0.0	3.39021	MLyα
46	5472.28	12.51±0.08	21.5± 5.4	3.53566	SiIII-1206
47	5473.70	12.64±0.06	31.8± 6.1	3.53683	SiIII-1206
48	5513.95	15.36±0.99	23.6± 7.8	3.53572	MLyα
49	5515.71	14.77±0.18	32.2± 3.0	3.53717	MLyα
50	5531.03	12.56±0.11	4.0± 2.4	3.38823	SiII-1260
51	5532.75	13.68±0.05	6.4± 0.9	3.38960	SiII-1260
52	5533.16	13.51±0.13	3.1± 1.3	3.38954	FeII-1260
53	5533.45	14.47±0.05	16.1± 1.3	3.39015	SiII-1260
54	5533.89	14.48±0.08	11.4± 1.0	3.39011	FeII-1260
55	5534.13	12.84±0.13	6.8± 3.4	3.39069	SiII-1260
56	5534.83	13.20±0.19	2.3± 0.7	3.39125	SiII-1260
57	5535.36	12.90±0.20	3.1± 2.0	3.39128	FeII-1260
58	5585.40	14.95±0.10	46.4± 4.6	3.59450	MLyα
59	5638.64	13.83±0.05	18.5± 3.7	3.53703	NV-1242
60	5706.37	12.77±0.13	1.7± 0.5	1.43423	FeII-2344
61	5714.27	13.58±0.10	14.2± 5.5	3.38826	OI-1302
62	5715.96	14.76±0.33	7.1± 2.3	3.38956	OI-1302
63	5716.71	15.12±0.49	15.7± 8.8	3.39014	OI-1302
64	5717.41	14.05±0.26	10.1± 5.6	3.39068	OI-1302
65	5723.89	12.56±0.11	4.0± 2.4	3.38823	SiII-1304
66	5725.67	13.68±0.05	6.4± 0.9	3.38960	SiII-1304
67	5726.39	14.47±0.05	16.1± 1.3	3.39015	SiII-1304
68	5727.09	12.84±0.13	6.8± 3.4	3.39069	SiII-1304
69	5727.82	13.20±0.19	2.3± 0.7	3.39125	SiII-1304
70	5771.04	15.23±0.37	20.5± 3.2	3.74721	MLyα
71	5814.30	12.60±0.04	11.1± 1.7	3.81914	SiIII-1206
72	5858.52	14.81±0.23	39.3± 8.0	3.81917	MLyα
73	5860.22	13.80±0.08	15.1± 3.1	3.39121	CII-1334
74	6105.79	12.41±0.04	13.8± 2.5	4.06074	SiIII-1206
75	6116.07	13.37±0.03	12.7± 0.8	3.38819	SiIV-1393
76	6117.19	13.44±0.02	21.2± 0.9	3.38899	SiIV-1393
77	6118.24	13.10±0.07	10.1± 2.1	3.38975	SiIV-1393
78	6118.72	13.43±0.18	10.8± 3.2	3.39010	SiIV-1393
79	6119.41	13.89±0.09	24.8± 6.8	3.39059	SiIV-1393
80	6120.27	13.60±14.85	15.0±102.	3.39120	SiIV-1393
81	6151.77	14.27±0.06	26.7± 3.9	4.06039	MLyα
82	6153.22	14.48±0.07	44.1± 7.3	4.06158	MLyα
83	6154.59	13.19±0.12	21.4± 5.6	4.06271	MLyα
84	6155.63	13.37±0.03	12.7± 0.8	3.38819	SiIV-1402
85	6156.75	13.44±0.02	21.2± 0.9	3.38899	SiIV-1402
86	6157.81	13.10±0.07	10.1± 2.1	3.38975	SiIV-1402
87	6158.30	13.43±0.18	10.8± 3.2	3.39009	SiIV-1402
88	6158.99	13.89±0.09	24.8± 6.8	3.39059	SiIV-1402
89	6159.86	13.60±14.85	15.0±102.	3.39120	SiIV-1402
90	6184.27	12.48±0.02	24.1± 1.7	4.12579	SiIII-1206
91	6193.76	12.46±0.03	16.6± 1.7	4.13365	SiIII-1206
92	6194.68	12.53±0.03	15.3± 1.6	4.13442	SiIII-1206
93	6201.22	14.40±0.02	28.2± 0.6	4.10106	MLyα
94	6231.52	13.76±0.03	29.4± 2.4	4.12599	MLyα
95	6232.78	12.85±0.06	17.9± 2.6	4.12703	MLyα
96	6236.02	15.02±0.22	24.0± 0.0	4.12970	MLyα
97	6237.67	15.80±0.93	27.8±15.6	4.13105	MLyα
98	6239.29	15.00±0.21	24.0± 0.0	4.13238	MLyα
99	6240.18	14.56±0.47	25.0± 0.0	4.13312	MLyα
100	6241.37	15.39±0.27	38.8± 3.1	4.13410	MLyα
101	6273.11	12.76±0.51	1.4± 5.1	3.05188	CIV-1548
102	6276.55	12.96±0.80	1.2± 1.3	3.05411	CIV-1548
103	6283.55	12.76±0.51	1.4± 5.1	3.05188	CIV-1550
104	6286.99	12.96±0.80	1.2± 1.3	3.05411	CIV-1550
105	6296.52	12.77±0.13	1.7± 0.5	1.43423	FeII-2586
106	6321.73	12.54±0.04	16.3± 2.1	3.53575	SiIV-1393
107	6323.42	12.59±0.04	17.0± 1.8	3.53696	SiIV-1393
108	6328.43	11.97±1.21	1.3± 1.1	1.43385	FeII-2600
109	6329.44	12.77±0.13	1.7± 0.5	1.43423	FeII-2600
110	6354.87	12.66±0.09	11.0± 3.6	4.12977	NV-1238
111	6356.46	13.15±0.04	23.9± 2.7	4.13105	NV-1238
112	6358.31	13.15±0.04	17.0± 2.3	4.13254	NV-1238
113	6360.42	13.53±0.03	34.9± 2.6	4.13424	NV-1238
114	6362.62	12.54±0.04	16.3± 2.1	3.53575	SiIV-1402
115	6364.32	12.59±0.04	17.0± 1.8	3.53696	SiIV-1402
116	6375.30	12.66±0.09	11.0± 3.6	4.12977	NV-1242
117	6376.90	13.15±0.04	23.9± 2.7	4.13105	NV-1242
118	6378.75	13.15±0.04	17.0± 2.3	4.13254	NV-1242
119	6380.86	13.53±0.03	34.9± 2.6	4.13424	NV-1242
120	6442.41	13.28±0.04	21.9± 3.0	3.16124	CIV-1548
121	6443.60	13.12±0.05	19.1± 2.9	3.16201	CIV-1548
122	6444.73	13.00±0.04	20.0± 0.0	3.16273	CIV-1548
123	6445.83	12.85±0.06	20.0± 0.0	3.16345	CIV-1548
124	6453.13	13.28±0.04	21.9± 3.0	3.16124	CIV-1550
125	6454.32	13.12±0.05	19.1± 2.9	3.16201	CIV-1550
126	6455.44	13.00±0.04	20.0± 0.0	3.16273	CIV-1550
127	6456.56	12.85±0.06	20.0± 0.0	3.16345	CIV-1550
128	6608.05	12.27±0.16	3.8± 5.5	1.77326	FeII-2382
129	6617.05	12.86±0.05	18.4± 2.8	3.74764	SiIV-1393
130	6659.85	12.86±0.05	18.4± 2.8	3.74764	SiIV-1402
131	6699.55	12.56±0.11	4.0± 2.4	3.38823	SiII-1526
132	6701.64	13.68±0.05	6.4± 0.9	3.38960	SiII-1526
133	6702.48	14.47±0.05	16.1± 1.3	3.39015	SiII-1526
134	6703.30	12.84±0.13	6.8± 3.4	3.39069	SiII-1526
135	6704.15	13.20±0.19	2.3± 0.7	3.39125	SiII-1526
136	6716.66	12.65±0.06	8.6± 2.3	3.81910	SiIV-1393
137	6760.10	12.65±0.06	8.6± 2.3	3.81910	SiIV-1402
138	6793.75	14.04±0.04	13.7± 1.0	3.38817	CIV-1548
139	6794.91	13.84±0.03	29.1± 3.3	3.38892	CIV-1548
140	6796.24	13.26±0.08	5.5± 2.3	3.38978	CIV-1548
141	6796.90	13.91±0.06	15.7± 2.2	3.39021	CIV-1548
142	6797.90	14.25±0.03	28.3± 2.5	3.39085	CIV-1548
143	6798.99	13.49±0.06	21.1± 2.5	3.39156	CIV-1548
144	6802.64	12.50±0.08	4.5± 1.5	1.43268	MgII-2796
145	6805.05	14.04±0.04	13.7± 1.0	3.38817	CIV-1550
146	6806.00	15.36±0.75	1.1± 5.7	1.43388	MgII-2796
147	6806.21	13.84±0.03	29.1± 3.3	3.38892	CIV-1550
148	6806.98	14.93±0.40	3.0± 0.4	1.43423	MgII-2796
149	6807.54	13.26±0.08	5.5± 2.3	3.38978	CIV-1550
150	6808.21	13.91±0.06	15.7± 2.2	3.39021	CIV-1550
151	6809.20	14.25±0.03	28.3± 2.5	3.39085	CIV-1550
152	6810.30	13.49±0.06	21.1± 2.5	3.39156	CIV-1550

Fig. 3. The Doppler parameter b as function of wavelength.

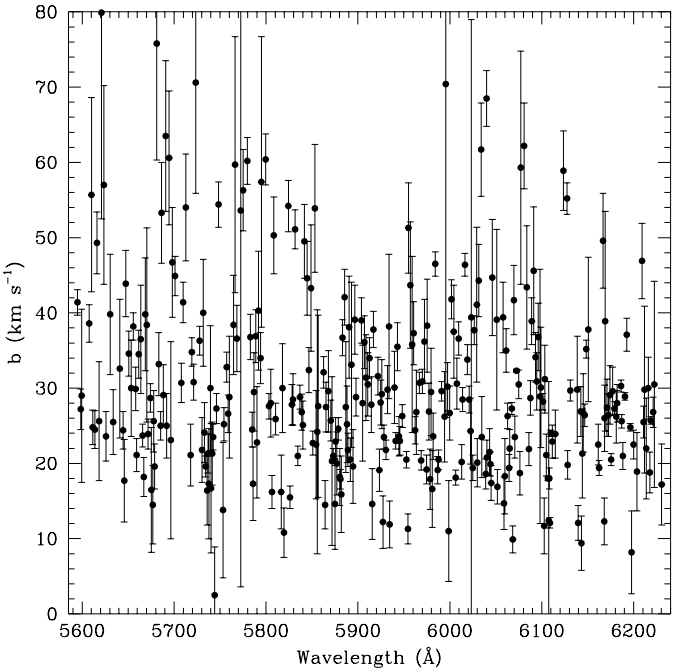

Fig. 4. The Doppler parameter distribution, with a median value of about 27.8 km s^{-1}. The lines are those not affected by the proximity effect.

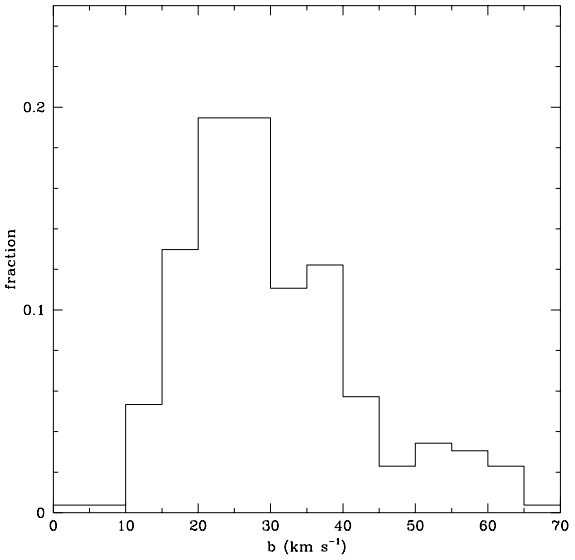

way the tendency of lines with larger b to show larger column densities is strongly reduced.

3.3. The UV background at $z \lesssim 4$

The reduction of the number density of the absorption lines along the wing of the quasar Lyα emission is interpreted as due to the enhancement of the ionization of the gas cloud by the UV emission of the nearby quasar which is superimposed to the general UV background (Bajtlik et al. 1988). This proximity effect allows a statistical estimate of the UVB as a function of redshift.

Following the Bajtlik et al. model, the line distribution per unit column density can be represented in the proximity of the QSO by (the subscript HI is omitted for simplicity):

$$\frac{\partial^2 n}{\partial z \partial N} = A(1+z)^{\gamma} N^{-\beta} (1+\omega)^{(1-\beta)} \ . \qquad (1)$$

where ω is the ratio of the quasar Lyman limit flux to the background flux received by any cloud at its redshift.

Assuming a power law spectrum $f_\nu \propto \nu^{-\alpha}$, with $\alpha = 0.72$ (Schneider et al. 1989) and the continuum flux estimated at the minimum between SiIV and CIV emissions from the spectrum of Schneider et al. 1989, the flux at 912 Å is $f_{912} = 2.5 \times 10^{-27}$ erg s^{-1} cm^{-2} Hz^{-1}. Uncertainties in the calculation of ω depend mainly on the estimate of the systemic emission redshift of the quasar. As shown by Espey et al. (1993), the best estimate of the actual redshift is given by the low ionization lines, as for example the MgII doublet. We adopted the value $z_{em} = 4.126$ as we derived from the fit to the OI(1302) emission line.

We have considered the sample of Lyα lines not associated with metal systems with $z \geq 3.60$ and $\log N_{HI} \geq 13.8$. The

Fig. 5. Plot of the Doppler parameter b versus $\log N_{HI}$ for a subsample of absorption lines. Solid dots are parameters obtained from a fit of the Lyα only, the squares show the result of the fit when Lyβ is also considered. One can note a splitting of the higher column density lines and a lowering of the b values.

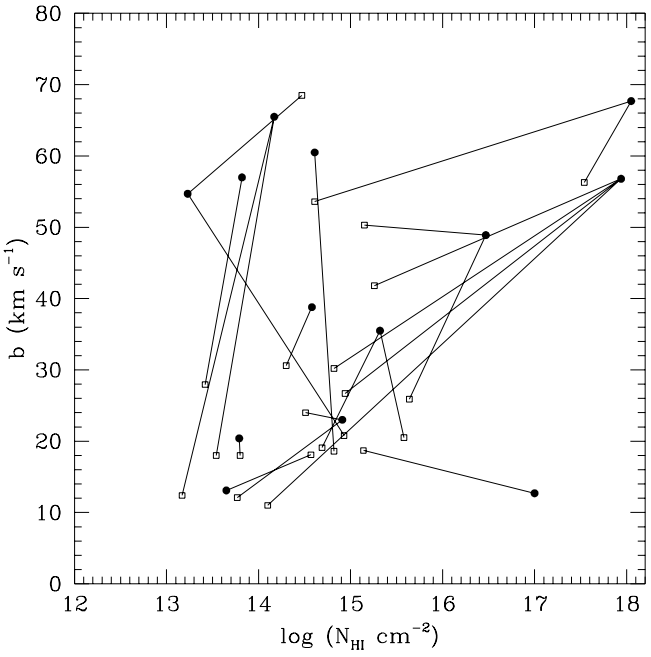

Fig. 6. $\partial n/\partial X_\gamma$ as function of $\log\omega$ for lines with $\log N_{HI} \geq 13.8$ and for the UV background radiation $J \simeq 7 \times 10^{-22}$ erg s^{-1} cm^{-2} Hz^{-1} sr^{-1}.

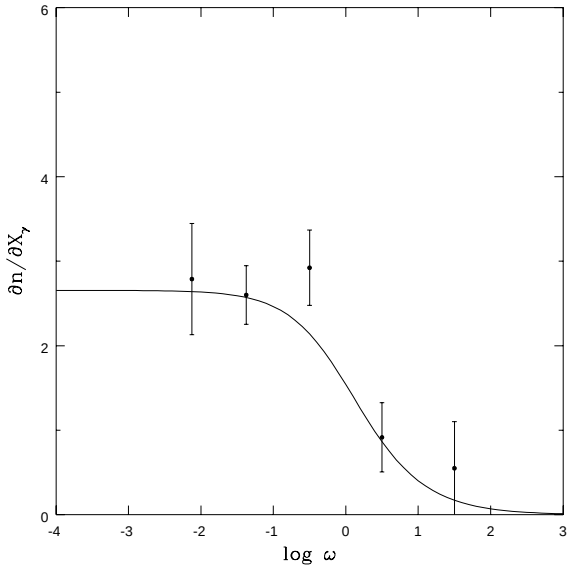

high threshold adopted for the column density of the sample avoids the bias in the redshift distribution of the weaker lines due to the blanketing effect produced by the stronger ones.

In Fig. 6 the predicted distribution of the line density in the coevolving redshift interval $dX_\gamma = (1+z)^\gamma$ is shown together with the data points binned as in Bajtlik et al. (1988). The best fit gives $J = J_{-22} \times 10^{-22}$ erg s^{-1} cm^{-2} Hz^{-1} sr^{-1} with $J_{-22} \simeq 7$ assuming an intrinsic line distribution with $\gamma = 2.89$, $\beta = 1.79$ and $A = 10^{11.22}$, as derived from the statistical analysis of the data sample used by Giallongo et al. (1996) for lines with $\log N_{HI} \geq 13.8$. Only values $J_{-22} < 4$ and $J_{-22} > 18$ are excluded at more than 2σ level. This result is consistent with the value $J_{-22} = 6$ derived from a large data sample (including this spectrum) by Giallongo et al. (1996) without correction for line blanketing. Including line blanketing corrections in the large sample reduces the UVB from $J_{-22} = 6$ to $J_{-22} = 5$. At higher redshift, $z \sim 4.5$, Williger et al. (1994), have measured the proximity effect in the forest of BR1033 − 03 obtaining a value $J_{-22} \sim 3$. This might imply a possible evolution of the UVB at $z > 4$, which is to be confirmed by a larger data set.

The value derived from the proximity effect in Q0000 − 26 is not far from that predicted for the quasar population at the same redshift $J_{-22} \sim 1 - 2$ (Haardt & Madau 1996), although there is room for a contribution by other kind of ionizing sources like primeval galaxies.

Disentangling between these two possibilities requires the knowledge of the shape of the UV background around the HeII edge at 4 Rydberg (228 Å). This can be done either through the direct measure of the quasar flux at 4 *Ryd* in the few cases where the quasar spectrum can be observed in this region (Jakobsen et al. 1994; Davidsen et al. 1995) or in an indirect way through the measure of the relative abundances of ions like CIV and SiIV whose ionization potentials are near the HeII edge (Miralda-Escudé & Ostriker 1990). In the next section we derive constraints on the shape of the UVB and on the nature of the ionizing sources from the study of three optically thin Lyα absorption systems at $z \gtrsim 3.5$.

4. The metal systems

The metal systems of 0000 − 26 have been already studied in Savaglio et al. (1994). In this work, the new data allow to confirm the old metal systems (except one) and to identify five new ones, with relatively low HI column density. Table 4 lists the two low redshift metal systems containing the MgII absorption doublet. Table 5 shows the CIV high-redshift systems with $z_{em} - z_{abs} > 5000$ km s^{-1}, considered to be intervening. Table 6 lists the CIV systems with $z_{em} - z_{abs} < 5000$ km s^{-1}, considered to be associated. All the high-redshift systems show CIV doublet together with the Lyα line.

For all the systems we looked for metal lines of cosmological relevance falling in the observed range. For most of these, we give upper limits to the column density assuming a b value as reported in the Tables. Statistical errors of the line parameters are given as a result of the line fitting procedure adopted.

4.1. Ionization in the intervening systems

QSO absorption systems showing metal lines are interpreted as originating in intervening galaxies and thus represent an important tool for the study of the chemical evolution of their gaseous content. The conversion of the observed column densities to the metal content of an optically thin gas cloud is not straightforward, since it depends on poorly known parameters, mainly the ionizing UV radiation and the cloud geometry and density. An extensive discussion on the chemical evolution of galaxies can be found in Timmes et al. (1995). Abundance determinations are traditionally reported in terms of an element abundance relative to iron, [X/Fe], as a function of the iron–to–hydrogen ratio [Fe/H]. The [Fe/H] ratio represents a chronometer in that the accumulation of iron in the interstellar medium increases monotonically with time. Unfortunately in the high redshift metal absorption systems iron is generally not observable, and abundances are derived respect to carbon and silicon.

Timmes et al. show that the [C/Fe] ratio is about constant within a large range of metallicity. Observations of halo Galactic stars give [C/Fe] ~ 0 down to [Fe/H] $= -2$ (Wheeler et al. 1989). For this reason carbon can be used, neglecting any depletion by dust, as a tracer of the chemical evolution of the absorbing clouds. Silicon is expected to be overabundant with respect to carbon by a factor not higher than [Si/C] $= 0.5 - 1$ *dex* as a result of nucleosynthesis of massive metal poor stars. Relative silicon determinations in the interstellar medium have been presented by Lu et al. (1996) for a sample of Damped Lyα systems. They found that in the range of metallicity $-2.6 <$ [Fe/H] < -0.7, there is a silicon overabundance respect to iron in the range [Si/Fe] $\sim 0.2 - 0.6$.

In this work we focus our attention to the metal systems which are optically thin in hydrogen, similar to those studied by Cowie et al. (1995), with HI column densities $\sim 10^{15}$ cm^{-2}.

In three cases we detected SiIV together with CIV absorption (Fig. 7). Their ratio provides an important information about the shape of the ionizing UV background and the sources responsible for it (Miralda-Escudé & Ostriker 1990). In particular the ratio depends on the average slope of the UVB around the HeII edge at 4 *Ryd*. Both model predictions and observations of far UV quasar spectra suggest that the UVB shape

Table 4. Low redshift metal systems of Q0000−26. Upper limits to column densities are obtained for b values between brackets.

z_{abs}	FeII		MgII		MgI	
	$\log N$	b	$\log N$	b	$\log N$	b
1.4326	13.47 ± 1.47	0.9 ± 0.4	12.50 ± 0.08	4.5 ± 1.5	< 12.0	(5)
1.4342	12.77 ± 0.13	1.7 ± 0.5	14.93 ± 0.40	3.0 ± 0.4	< 11.7	(5)
1.4338	11.97 ± 1.21	1.3 ± 1.1	15.36 ± 0.75	1.1 ± 5.7	< 11.4	(5)
1.7732	< 12.7	(10)	12.43 ± 0.25	2.4 ± 2.5	< 11.6	(10)
1.7736	< 12.5	(10)	13.50 ± 1.79	1.6 ± 0.7	< 11.6	(10)

Fig. 7. SiIV, CIV and HI absorption for three intervening systems, one of which with two components.

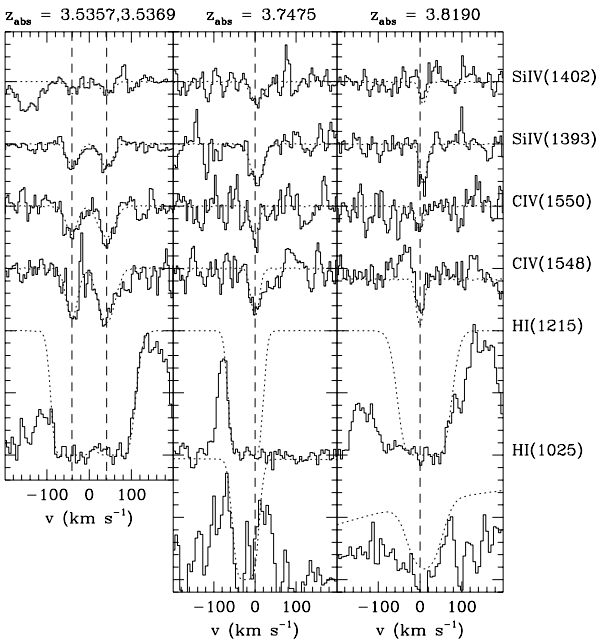

beyond 1 *Ryd* is more complex than a simple power law because of HI and HeII absorption by the intergalactic medium (Madau 1992). An intrinsic steepening of the UVB at the HeII edge could be also present if the ionizing sources are of stellar origin.

In this discussion we considered all absorption lines in every metal component having origin in a single–phase gas cloud, with a uniform density and ionization state.

We assumed that the UV background radiation is the only ionizing source. Thus the large b values found in some system suggest the presence of additional broadening mechanisms, like turbulent broadening or the presence of several components, which cannot be constrained given the limited s/n and resolution. Nevertheless, we have verified that adding components or a turbulent broadening does not change significantly the total CIV and SiIV column densities, as expected for unsaturated lines.

To estimate absolute and relative abundances for the three systems, we used the standard photoionization code CLOUDY (Ferland 1991) varying the most critical parameters like the intensity and shape of the UVB and the total density of the clouds.

We considered two values for the UV flux at 912 Å, $J_{-22} = 1$ and 5. For each of the four components at z_{abs}= 3.5357, 3.5369, 3.7475 and 3.8190 we have computed the metallicity [C/H] and the relative abundance [C/Si] respect to solar values as a function of the total density assuming different UVB shapes. The HI column densities assumed are those derived from the fit of the Lyα and/or Lyβ shown in Fig. 7. An upper limit can be estimated from the lack of the Lyman limit edge (Fig. 9) to be $\log N_{HI} \lesssim 16$.

Results are shown in Fig. 8 for $J_{-22} = 5$ and different assumptions on the jump at the HeII edge $S_L \equiv J(1Ryd)/J(4Ryd)$. In the first plots from the left the value $S_L = 25$ is assumed according to the predicted shape of the UVB produced by quasars (Haardt & Madau 1996). In the other cases, progressively higher values are assumed as expected when stellar ionizing sources become the dominant contributors.

In all the systems shown in Fig. 8 it appears that when $\log S_L < 2$, the [C/Si] ratio can be maintained within acceptable values higher than -1 *dex*, in agreement with prediction by chemical evolution models for galaxies (Timmes et al. 1995), only for $\log n_H \gtrsim -2.5$. At such high densities the metallicity is relatively high [C/H] $= -1 \sim -1.5$, while the cloud thickness is of only few hundreds of parsec. If we assume sizes at least one order of magnitude larger (few kpc) we are forced to lower the density of the systems to $\log n_H = -3$ resulting in an implausible overabundance of silicon over carbon by 100–1000 times the solar value.

However, if we assume a deeper UVB jump at the HeII edge we can obtain more consistent results. For $S_L \gtrsim 1000$ the silicon overabundance is within a factor of 10 in all the systems considered and the metallicities are about two orders of magnitude below the solar, while keeping the cloud size reasonably large.

Similar results hold also for $J_{-22} = 1$, where we have in general higher values of [C/H] and [C/Si]. For $S_L \lesssim 100$ we have [C/Si] ~ -1 for $\log n_H \sim -3$, but the sizes remain less than a kpc and the metallicities would be unusually high, [C/H] $\gtrsim -1$, for these optically thin clouds.

Errors on the abundance determinations are mostly systematic and due to uncertainties on the model. However, uncertainties coming from the fitting procedure are dominated by errors on the HI column density, since these are much larger than for metal lines. We have verified that relative metal abun-

Table 5. Intervening metal systems. Upper limits to column densities are obtained for b values between brackets. Detections reported with an asterisk are doubtful because in the Lyα forest or very weak. The reported redshifts are referred to the CIV doublet.

z_{abs}	HI		CIV		CII		CI		SiIV		SiIII		SiII	
	$\log N$	b	$\log N$	b	$\log N$	b	$\log N$	b	$\log N$	b	$\log N$	b	$\log N$	
3.05189	–	–	12.76 ± 0.51	1.4 ± 5.1	< 13.4	(20)	< 13.2	(20)	< 13.3	(40)	< 13.1	(20)	< 12.6	
3.05411	20.2 ± 0.1	–	12.96 ± 0.80	1.2 ± 1.3	< 14.6	(21)	< 13.2	(20)	< 13.2	(20)	< 13.0	(20)	< 12.6	
3.16124	15.88 ± 1.44	$16.2 \pm 5.9*$	13.28 ± 0.04	21.9 ± 3.0	< 13.7	(20)	< 13.2	(20)	< 14.6	(40)	12.93 ± 0.13	$8.2 \pm 2.5*$	< 12.6	
3.16201	15.39 ± 4.00	$15.1 \pm 3.2*$	13.12 ± 0.05	19.1 ± 2.9	< 14.5	(20)	< 13.2	(20)	< 14.6	(25)	13.18 ± 0.06	$24.7 \pm 5.5*$	< 13.1	
3.16274	15.99 ± 0.63	$15.8 \pm 4.6*$	13.00 ± 0.04	(20)	< 13.6	(20)	< 13.2	(20)	< 14.6	(25)	12.55 ± 0.24	$15.9 \pm 10.1*$	< 12.7	
3.16345	15.37 ± 0.63	$15.1 \pm 2.5*$	12.85 ± 0.06	(20)	< 13.8	(20)	< 13.2	(20)	< 14.4	(20)	13.00 ± 0.03	$27.8 \pm 2.6*$	< 13.3	
3.38818	–	–	14.04 ± 0.04	13.7 ± 1.0	< 14.2	(20)	< 13.3	(20)	13.37 ± 0.03	12.7 ± 0.8	< 13.9	(20)	12.56 ± 0.11	4.0
3.38892	–	–	13.84 ± 0.03	29.1 ± 3.3	< 14.7	(20)	< 13.3	(20)	13.44 ± 0.02	21.2 ± 0.9	< 17.0	(20)	< 12.8	
3.38978	–	–	13.26 ± 0.08	5.5 ± 2.3	< 17.0	(20)	< 13.3	(20)	13.10 ± 0.07	$10.1 \pm 2.1*$	< 16.7	(20)	13.68 ± 0.05	6.4
3.39021	21.3 ± 0.1	–	13.91 ± 0.06	15.7 ± 2.2	< 17.0	(20)	< 13.3	(20)	13.43 ± 0.18	$10.8 \pm 3.2*$	< 14.8	(20)	14.47 ± 0.05	16.
3.39085	–	–	14.25 ± 0.03	28.3 ± 2.5	< 14.2	(20)	< 13.3	(20)	13.89 ± 0.09	$24.8 \pm 6.8*$	< 13.2	(20)	12.84 ± 0.13	6.8
3.39156	–	–	13.49 ± 0.06	21.1 ± 2.5	13.80 ± 0.08	$15.1 \pm 3.1*$	< 13.3	(20)	13.60 ± 14.85	(15)*	< 14.7	(20)	13.20 ± 0.19	2.3
3.53572	14.77 ± 0.18	32.2 ± 3.0	13.32 ± 0.05	16.6 ± 3.2	< 13.0	(20)	< 13.3	(20)	12.54 ± 0.04	16.3 ± 2.1	12.51 ± 0.08	21.5 ± 5.4	< 13.2	
3.53696	15.36 ± 0.99	23.6 ± 7.8	13.53 ± 0.03	24.7 ± 2.5	< 13.0	(20)	< 13.3	(20)	12.59 ± 0.04	17.0 ± 1.8	12.64 ± 0.06	31.8 ± 6.2	< 12.9	
3.59452	14.95 ± 0.10	46.4 ± 4.6	13.35 ± 0.05	25.9 ± 3.5	< 13.7	(20)	13.07 ± 0.22	$11.6 \pm 9.1*$	< 12.2	(20)	< 12.3	(20)	< 12.6	
3.74757	15.23 ± 0.37	20.5 ± 3.2	13.20 ± 0.12	11.5 ± 3.3	< 12.9	(20)	< 13.4	(20)	12.86 ± 0.05	18.4 ± 2.8	< 13.4	(20)	< 13.0	
3.81900	14.81 ± 0.23	39.3 ± 8.0	13.08 ± 0.08	8.6 ± 3.2	< 13.0	(10)	< 13.4	(20)	12.65 ± 0.06	8.6 ± 2.3	12.60 ± 0.04	11.1 ± 1.7	< 12.8	

z_{abs}	NV		NI		AlIII		AlII		FeII		OI		MgI	
	$\log N$	b	$\log N$	b	$\log N$	b	$\log N$	b	$\log N$	b	$\log N$	b	$\log N$	b
3.05189	< 13.3	(20)	< 14.3	(20)	< 12.2	(20)	< 12.0	(20)	< 13.2	(20)	< 14.3	(13)	< 13.2	(20)
3.05411	< 13.3	(20)	< 15.0	(20)	< 12.2	(20)	< 12.0	(20)	< 13.2	(20)	< 15.2	(36)	< 13.5	(20)
3.16124	< 14.0	(20)	< 14.3	(20)	< 12.4	(20)	< 11.9	(20)	< 13.5	(20)	< 13.9	(20)	< 14.7	(20)
3.16201	< 13.2	(20)	< 13.7	(20)	< 12.4	(20)	< 11.9	(20)	< 13.4	(20)	< 13.8	(20)	< 14.0	(20)
3.16274	< 13.3	(20)	14.0	(20)	< 12.4	(20)	11.86 ± 0.11	$4.7 \pm 8.6*$	< 13.3	(20)	< 13.6	(20)	< 13.8	(20)
3.16345	< 14.0	(20)	14.7	(20)	< 12.4	(20)	< 11.9	(20)	< 13.5	(20)	< 13.8	(20)	< 14.5	(20)
3.38818	< 13.4	(20)	< 14.3	(20)	< 12.6	(20)	< 11.8	(20)	< 13.4	(20)	13.58 ± 0.10	14.2 ± 5.5	< 13.8	(20)
3.38892	< 13.6	(20)	< 14.4	(20)	< 12.7	(20)	< 11.8	(20)	< 13.4	(20)	< 13.2	(20)	< 13.8	(20)
3.38978	< 13.6	(20)	< 14.1	(20)	< 12.6	(20)	11.89 ± 0.14	10.5 ± 6.1	13.51 ± 0.13	3.1 ± 1.3	14.76 ± 0.33	7.1 ± 2.3	< 13.8	(20)
3.39021	< 13.7	(20)	14.69 ± 0.04	13.9 ± 1.3	< 12.8	(20)	13.15 ± 0.14	13.7 ± 2.1	14.48 ± 0.08	11.4 ± 1.0	15.12 ± 0.49	15.7 ± 8.8	< 13.7	(20)
3.39085	< 13.9	(20)	< 14.1	(20)	< 12.8	(20)	11.60 ± 0.25	2.5 ± 3.4	< 13.1	(20)	14.05 ± 0.26	10.2 ± 5.6	< 13.6	(20)
3.39156	< 14.7	(20)	< 14.1	(20)	< 12.6	(20)	12.09 ± 0.10	17.3 ± 6.4	12.90 ± 0.20	3.1 ± 2.0	< 14.0	(20)	< 13.6	(20)
3.53572	< 13.2	(20)	< 14.2	(20)	< 12.8	(20)	12.07 ± 0.12	29.7 ± 9.8	< 13.2	(20)	< 14.9	(32)	< 13.8	(20)
3.53696	13.83 ± 0.05	$18.5 \pm 3.7*$	< 14.0	(20)	< 12.8	(20)	< 11.8	(20)	< 13.2	(20)	< 15.0	(20)	< 13.8	(20)
3.59452	< 14.1	(20)	< 14.3	(20)	< 13.0	(20)	< 12.4	(20)	< 13.4	(20)	< 14.3	(20)	< 14.1	(20)
3.74757	< 13.1	(20)	< 13.4	(20)	< 13.3	(20)	< 11.9	(20)	< 13.8	(20)	< 14.3	(20)	< 14.8	(20)
3.81900	< 13.4	(20)	< 13.8	(20)	< 13.4	(20)	< 12.1	(20)	< 13.6	(20)	< 13.0	(20)	< 14.3	(20)

Table 6. Associated metal systems. Upper limits to column densities are obtained for b values between brackets. Detections reported with an asterisk are doubtful because in the Lyα forest or very weak. The reported redshifts are referred to the CIV doublet.

z_{abs}	HI		CIV		CIII		CII		CI		SiIV		SiIII		SiII	
	$\log N$	b	$\log N$	b	$\log N$	b	$\log N$	b	$\log N$	b	$\log N$	b	$\log N$	b	$\log N$	b
4.06064	14.27 ± 0.06	26.7 ± 3.9	13.24 ± 0.16	32.4 ± 15.4	< 13.5	(20)	< 13.2	(20)	< 13.3	(20)	12.49 ± 0.09	6.9 ± 3.7	12.41 ± 0.04	13.8 ± 2.5	< 12.4	(2
4.06157	14.48 ± 0.07	44.1 ± 7.3	13.47 ± 0.09	19.3 ± 4.2	< 14.0	(20)	< 13.2	(20)	< 13.7	(20)	< 12.5	(20)	< 13.3	(20)	< 12.2	(2
4.06248	13.19 ± 0.12	21.4 ± 5.6	13.26 ± 0.09	23.1 ± 6.7	< 13.4	(20)	< 13.2	(20)	< 13.2	(20)	< 12.6	(20)	< 12.9	(20)	< 12.5	(2
4.10106	14.40 ± 0.02	28.2 ± 0.6	13.21 ± 0.04	12.5 ± 2.0	< 13.4	(20)	< 13.7	(20)	< 14.0	(20)	12.39 ± 0.15	5.3 ± 3.5	< 13.1	(20)	< 12.3	(2
4.12605	13.76 ± 0.03	29.4 ± 2.4	13.54 ± 0.03	16.7 ± 1.7	< 13.5	(20)	< 13.2	(20)	< 13.6	(20)	< 12.7	(20)	12.48 ± 0.02	$24.1 \pm 1.7*$	< 12.4	(2
4.12688	12.85 ± 0.06	17.9 ± 2.6	13.17 ± 0.05	10.0 ± 2.2	< 13.8	(20)	< 13.3	(20)	< 13.6	(20)	< 12.5	(20)	< 13.2	(20)	< 12.3	(2
4.12983	15.02 ± 0.22	24.0 ± 3.0	13.46 ± 0.04	11.8 ± 1.7	< 13.4	(20)	< 13.1	(20)	< 13.5	(20)	< 12.5	(20)	< 12.2	(20)	< 12.4	(2
4.13111	15.80 ± 0.93	27.8 ± 15.6	14.34 ± 0.05	16.7 ± 0.8	< 14.4	(20)	< 13.1	(20)	< 13.5	(20)	12.75 ± 0.07	18.5 ± 5.3	< 13.4	(30)	< 12.2	(2
4.13245	15.00 ± 0.21	(24)	14.62 ± 0.13	15.8 ± 1.3	14.22 ± 0.25	$16.0 \pm 2.2*$	< 13.1	(20)	< 13.4	(20)	12.49 ± 0.10	13.9 ± 6.2	< 12.1	(15)	< 12.4	(2
4.13331	14.56 ± 0.47	(25)	13.68 ± 0.07	8.1 ± 2.1	< 13.8	(20)	< 13.1	(20)	< 13.5	(20)	12.40 ± 0.11	(15)	12.46 ± 0.03	16.6 ± 1.7	< 12.4	(2
4.13420	15.39 ± 0.27	38.8 ± 3.12	14.51 ± 0.03	29.8 ± 1.6	< 14.4	(20)	< 13.1	(20)	< 13.5	(20)	12.98 ± 0.06	30.0 ± 4.6	12.53 ± 0.03	15.3 ± 1.6	< 12.4	(2

z_{abs}	NV		NIII		NI		AlII		FeIII		FeII		OVI		OI	
	$\log N$	b	$\log N$	b	$\log N$	b	$\log N$	b	$\log N$	b	$\log N$	b	$\log N$	b	$\log N$	b
4.06064	< 12.9	(20)	< 14.6	(20)	< 14.6	(20)	< 12.6	(20)	< 14.9	(20)	< 13.5	(20)	< 13.4	(20)	–	–
4.06157	< 12.9	(20)	–	–	< 13.5	(20)	< 12.4	(20)	< 14.7	(20)	< 13.5	(20)	< 13.9	(20)	–	–
4.06248	< 12.9	(20)	< 15.4	(20)	< 13.6	(20)	< 12.5	(20)	< 14.7	(20)	< 13.5	(20)	< 14.1	(25)	–	–
4.10106	< 12.7	(20)	< 14.4	(24)	< 13.0	(20)	< 12.5	(20)	< 14.2	(24)	< 13.4	(20)	14.41 ± 4.67	$2.1 \pm 8.5*$	< 13.3	(20)
4.12605	< 12.8	(20)	< 14.0	(20)	< 13.8	(20)	< 12.7	(20)	< 14.2	(24)	< 13.5	(20)	< 14.7	(24)	< 13.4	(20)
4.12688	< 12.7	(20)	< 13.7	(20)	< 13.8	(20)	< 12.7	(20)	< 13.7	(20)	< 13.7	(20)	< 14.5	(24)	< 13.4	(20)
4.12983	12.66 ± 0.09	11.0 ± 3.6	< 13.6	(20)	< 13.9	(20)	< 12.8	(20)	< 14.4	(20)	< 13.7	(20)	14.48 ± 0.93	$5.8 \pm 3.1*$	< 13.4	(20)
4.13111	13.15 ± 0.04	23.9 ± 2.7	< 13.7	(20)	< 13.6	(20)	< 12.8	(20)	< 13.8	(20)	< 13.7	(20)	17.00 ± 0.28	$23.3 \pm 4.4*$	< 13.4	(20)
4.13245	13.15 ± 0.04	17.0 ± 2.3	< 14.1	(20)	< 14.3	(20)	< 12.8	(20)	< 13.3	(20)	< 13.5	(20)	16.18 ± 2.83	$10.6 \pm 8.6*$	< 13.4	(20)
4.13331	< 12.8	(20)	< 14.7	(20)	< 14.3	(20)	< 12.8	(20)	< 13.2	(20)	< 13.7	(20)	14.25 ± 5.81	$3.2 \pm 7.5*$	< 13.5	(20)
4.13420	13.53 ± 0.03	34.9 ± 2.6	< 14.0	(20)	< 14.2	(20)	< 12.8	(20)	< 13.8	(20)	< 13.7	(20)	17.00 ± 0.02	$18.0 \pm 0.7*$	< 13.7	(20)

Fig. 8. Metal content as function of the gas density for three intervening systems (one of which with two components) with HI, CIV and SiIV absorption. Here we assume $J_{-22} = 5$ and varied S_L. Error bars for [C/H] due to the errors on the column densities of HI and CIV are of about 0.2 *dex*, 1 *dex*, 0.5 *dex* and 0.3 *dex* for the four systems at $z = 3.5357,\ 3.5369,\ 3.7475,\ 3.8190$ respectively. Error bars for relative abundances of [C/Si] are typically of 0.1 *dex*.

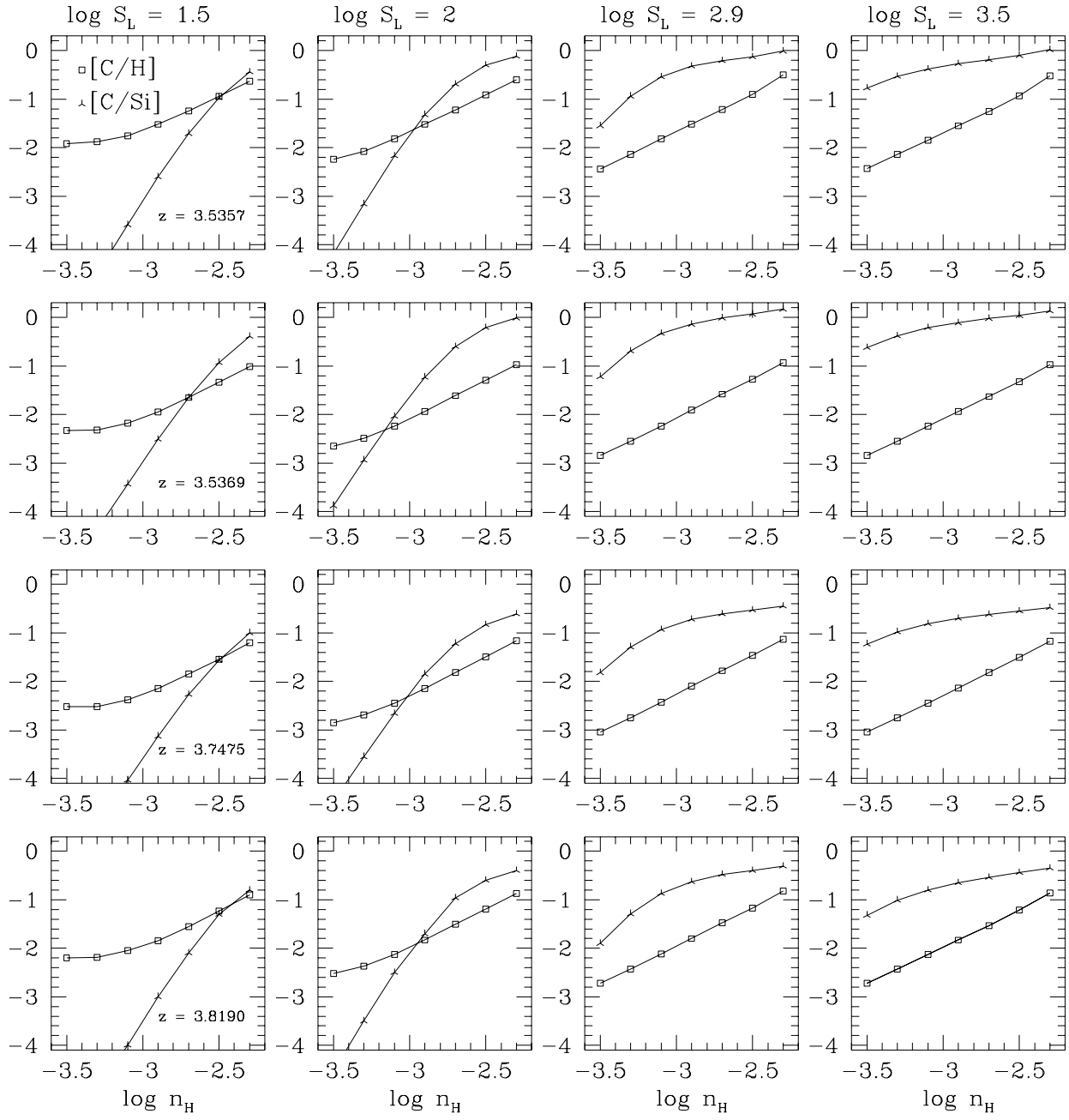

dances do not change rescaling the HI column density according to the upper and lower limit given by the errors, while the metallicity do.

We notice that Songaila et al. (1995) have observed four metal systems in the spectrum of 2000–33 deriving an average $S_L \sim 70$ at $z = 3.2$. Any further constraint on the shape of the UV flux coming from the ionization state of low column density Lyα lines will be important for the investigation of the evolution with redshift or inhomogeneity of the ionizing UV population.

At this point we can only speculate that being the IGM highly ionized at the Lyman limit as derived by the Gunn-Peterson test in the spectra of the highest redshift quasars known (Giallongo et al. 1994), the UVB should maintain a high intensity level beyond 1 *Ryd* up to $z = 5$. Since the number density of quasars at redshift $z > 3$ bends down (Pei 1995), a

change in the kind of ionizing population could take place at these redshifts with a possible dominance of primeval galaxies. Given the strong spectral difference at the HeII edge of the two populations, an increasing jump at the HeII edge with increasing redshift should be expected.

Fig. 9. Portion of the long slit spectrum at low resolution. Ticks show the position of Lyman limits for some of the detected metal systems.

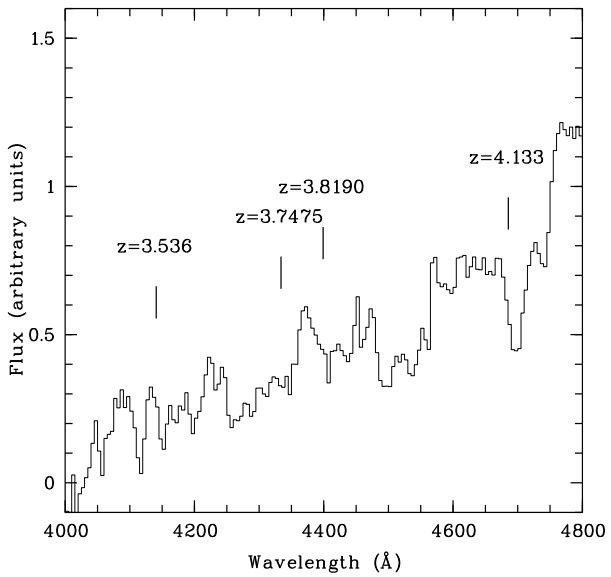

4.2. The associated systems

The abundances of the associated system have been determined in few cases and in all of them high ionization with high metal content has been derived (Møller et al. 1993; Wampler et al. 1993; Savaglio et al. 1994; Petitjean et al. 1994). In all these measurements different shapes have been assumed for the ionizing background, and this is presumably dominated by the flux of the QSO itself.

Indeed the distance of the cloud cannot be derived in a straightforward way because of the uncertainty in the measure of the systemic redshift and because of the importance of the cloud peculiar motions.

We found four associated systems, with a total of 11 components (Table 6). We estimate the metal abundances varying the intensity of the ionizing source using different values of the ionization parameter U. We assumed a simple power-law spectrum with spectral index $\alpha = 1.5$ ($f_\nu \propto \nu^{-\alpha}$). Also a value $\alpha = 0.72$ has been considered. The first value is a reasonable assumption for frequencies $\nu \geq 4$ *Ryd* ($\lambda \leq 228$ Å), relevant for the considered ions, to keep the flux of the object at low values at X–ray frequencies. The second value is that used for the proximity effect and is more appropriate for $\nu \leq 1$ *Ryd* ($\lambda \geq 912$ Å).

As for the intervening systems, all the absorption lines in every metal component are assumed to be originated in a single–phase gas cloud, with a uniform density and ionization state. The model results are shown in Fig. 10 for five of the 11 measured components where the presence of silicon and/or nitrogen provides some constraints to the models.

For the strongest system at $z \sim 4.13$ the metal content of the third and fourth component is omitted because the relevant HI column densities are particularly uncertain due to the saturated and blended profile of the Lyα lines. The Lyβ lines fall in the blue wing of the damped Lyα line at z_{abs}= 3.39, making the line fitting more complicated. The total HI column density is $\log N_{HI} \simeq 16.2$. From our grism spectrum we estimate an upper limit to the HI optical depth at 912 Å (Fig. 9), corresponding to a total HI column density $\log N_{HI} \lesssim 16$, consistent with the value found from our best fit. The OVI column densities reported in Table 6 are probably upper limits because of the confusion with the Lyα forest and with the blue wing of the damped Lyα line at z_{abs}= 3.39. For the three components considered in this analysis, results from the fit give ratios of the HI to OVI of $\log(N_{HI}/N_{OVI}) \simeq -1.8, -3.9, -3.5$ respectively, suggesting the OVI contamination.

Concerning the other three systems at lower redshifts, only the first component of the system at $z \simeq 4.06$ shows SiIII and SiIV together with CIV. The SiIV line is observed also in the system at $z = 4.1010$. For the system at $z = 4.126$ we only give for the first component an upper limit to the SiIV abundance and a tentative SiIII identification in the Lyα forest.

In Fig. 10 we show CLOUDY results for the selected components of the associated systems. We report the metal abundances ([C/H]) and the relative abundance of nitrogen and silicon respect to carbon as a function of the ionization parameter U. The adopted gas density is $\log n_H = -2$ and the quasar spectral index is $\alpha = 1.5$.

Constraints to the model can be derived from the upper limits on CIII and from the detection of silicon. The upper limit to the column density of CIII gives a lower limit to the ionization parameter and an upper limit to the metallicity. The only exception is the $z = 4.0606$ system for which we can only say that [C/Si] > -1 gives [C/H] > -0.7 and that the observed CIV can be reproduced only for $\log U > -2.4$

For the system at $z = 4.1010$ the limits are $\log U > -2.3$ and [C/H] < -0.3. If we require a relative silicon abundance lower than 1 *dex*, the metallicity is [C/H] $\simeq -1$ and $\log U < -1.9$.

In the system at $z = 4.1298$, the non detection of CIII implies $\log U > -1.9$ and consequently [C/H] < -1.3. The nitrogen relative abundance remains close to that solar.

In the system at $z = 4.1311$, the upper limit to the CIII column density gives $\log U > -2.1$ and [C/H] < -0.9. The relative silicon abundance is lower than 1 *dex* if [C/H] > -1.5. For $-1.5 <$ [C/H] < -0.9, the relative nitrogen abundance is $-0.4 <$ [N/C] < -0.2. In the last component, at $z = 4.1342$, $\log U > -2.1$ and consequently [C/H] < -0.3. From the relative silicon abundance we derive [C/H] > -0.9. In this range of metallicity, the nitrogen abundance is $-0.3 <$ [N/H] < 0.0.

As for the intervening systems, errors on the HI column densities are much larger than for metal lines and relative metal abundances do not change rescaling the HI column density according to the upper and lower limit given by the errors, while the metallicity do.

From the analysis with $\alpha = 1.5$, we conclude that in the detected metal systems the metallicity is undersolar, although values lower than [C/H] ~ -1 are unlikely. This value is about one order of magnitude higher than that found in intervening systems at about the same redshift. A silicon overabundance

Fig. 10. Metal content as function of the ionization parameter for five associated systems. We assume $\log n_H = -2$ and $\alpha = 1.5$. Errors bars for [C/H] due to the errors on the column densities of HI and CIV are of about 0.2 *dex*, 0.06 *dex*, 0.3 *dex*, 1 *dex* and 0.3 *dex* for the five systems from the left to the right of the figure. Error bars for relative abundances of [C/Si] and [N/C] are typically of 0.1 *dex*.

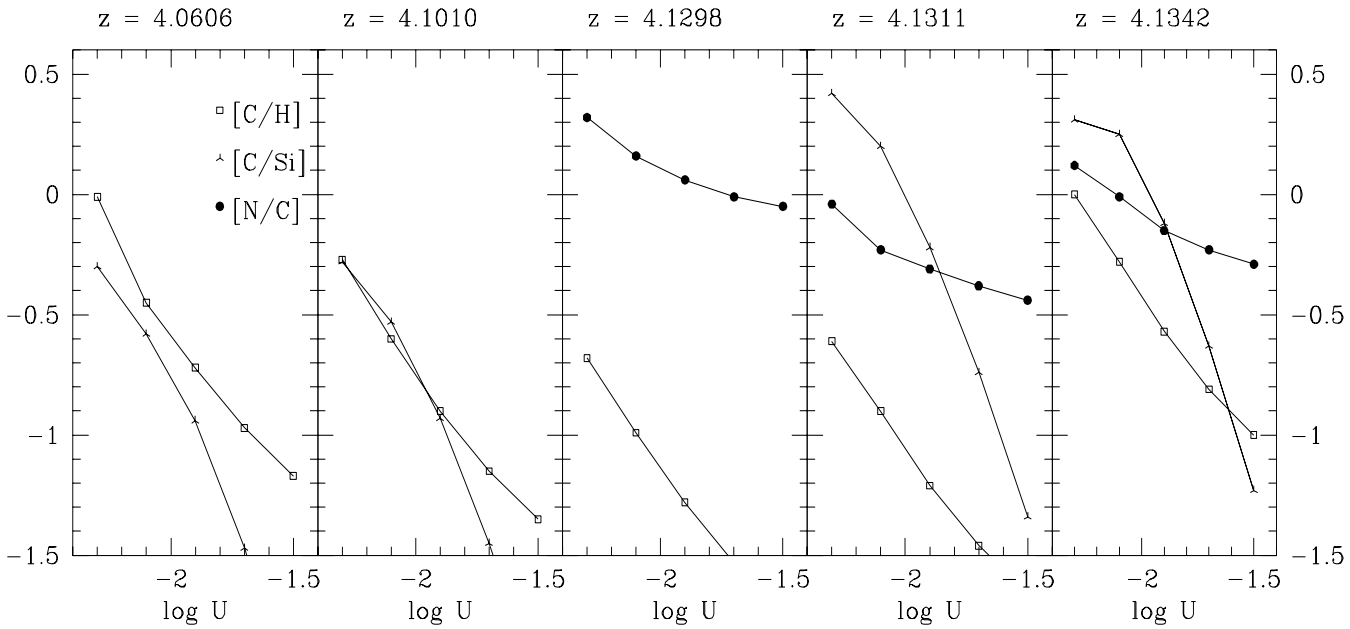

seems favoured, while the nitrogen abundance tends to be undersolar.

For $\alpha = 0.72$, the values of [C/H] are higher with respect to the previous analysis, up to 0.2 *dex* for the considered lower limit in the $\log U$ and of the order of 0.6 *dex* for the upper limit of $\log U$. The [N/C] values are slightly lower, while the Silicon overabundance results much higher, being almost in all cases higher by 1 *dex*.

Savaglio et al. (1994) reported slightly higher values for the metallicity of the same associated systems. The greater wavelength coverage, the better s/n of the present data and the new line fitting procedure adopted, allow a more accurate estimates of the line parameters. Moreover it was possible to detect new absorption lines and to infer more stringent upper limits to non–detected lines. In particular new upper limits on CIII absorptions have been used to derive upper limits on the metallicity. In this work we also used a more accurate photoionized code and we excluded the possibility of having silicon overabundances higher by 1 *dex*, lowering the upper limit to the metallicity. Finally, we have focused our attention on those systems for which we have reliable information only.

Metallicities derived for associated systems in $z_{em} = 2 - 3$ quasars show nearly solar values and in some cases even higher than solar (Wampler et al. 1993; Petitjean et al. 1994; Møller et al. 1994). The lower metallicities derived for some systems at $z \simeq 4$ might be indicative of an evolution with redshift of the chemical abundances in the associated systems, which however needs confirmation with a larger sample of high quality data.

5. Summary

We have presented a list of absorption lines observed in the spectrum of the quasar Q0000 − 2619 ($z_{em} = 4.126$) with a resolution of 13 km s^{-1} and a signal–to–noise ratio of 15 − 60 per resolution element. The main results of the statistical analysis can be summarized as follows:

- The mode of the Doppler distribution for the Lyα lines is $\simeq 25$ km s^{-1} with a dispersion of 7 km s^{-1}. The fraction of line with $10 < b < 20$ km s^{-1} is 17%. The Doppler values derived from uncontaminated Lyβ lines are smaller than those obtained from the corresponding Lyα, suggesting the contribution of non saturated, non resolved components in the Lyα profiles.
- On the basis of the proximity effect in this spectrum the integrated UV background is estimated to be $J \sim 7 \times 10^{-22}$ erg s^{-1} cm^{-2} Hz^{-1} sr^{-1}, although only values of $J_{-22} < 4$ and $J_{-22} > 18$ are excluded at more than 2σ level. This value is consistent with previous estimates obtained at a lower z, implying no appreciable redshift evolution of the UVB up to $z = 4$, in agreement with the absence of any Gunn-Peterson effect up to $z = 5$.
- The analysis of the intervening metal line systems has revealed in particular the presence of three optically thin systems with $\log N_{HI} \sim 15$ showing associated CIV and SiIV absorptions. [Si/C] ratios lower than 10 times the solar value can be obtained only assuming a large jump in the spectrum of the ionizing UV background beyond the HeII edge ($J_{912}/J_{228} \gtrsim 1000$). This result, if confirmed in other spectra at the same redshift, is suggestive of a possible in-

crease of the stellar ionizing emissivity over the declining quasar one for $z > 3$.

– The analysis of the associated metal line systems suggests abundances generally below solar with typical values in the range $0 <$ [C/H]< -1. The derived values are lower than those estimated for associated systems found in lower z quasars.

Acknowledgements. It is a pleasure to thank M. Limongi and G. Marconi for useful remarks on an early version of the paper. S.S. acknowledges the kind hospitality at the Osservatorio Astronomico di Roma where most of this work was done.

References

Bahcall J. N., et al., 1996, ApJ, 457, 19.
Bajtlik, S., Duncan, R. C., Ostriker, J. P. 1988, ApJ, 327, 570.
Bergeron J., Boissé P., 1991, A&A, 243, 344.
Bergeron J., Cristiani S., Shaver, P. A., 1992, A&A, 257, 417.
Carswell R. F., 1995, *Proceedings of the ESO Workshop on Quasars Absorption Lines*, ed. G. Meylan, p313.
Charlton J. C., 1995, *Proceedings of the ESO Workshop on Quasars Absorption Lines*, ed. G. Meylan, p405.
Chernomordik V. V., 1995, ApJ, 440, 431.
Cowie L. L., Songaila A., Kim T.-S., Hu E. M., 1995, AJ, 109, 1522.
Cristiani S., D'Odorico S., D'Odorico V.,Fontana A., Giallongo E., Savaglio S., 1996, MNRAS, *submitted*.
Cristiani, D'Odorico, S., Fontana, A, Giallongo, E., Savaglio, S., 1995, MNRAS, 273, 1016.
Davidsen A. F., Kriss G. A., Zheng W., 1996, Nat, 380, 47.
D'Odorico, S. 1990, *ESO The Messenger*, 61, 51.
Espey, B. R. 1993, ApJL, 411, 59.
Ferland G. J., 1991, *OSU Astronomy Dept. Internal Rept.*, 91-01
Fernández–Soto A., Lanzetta K. M., Barcons X., Carswell R. F., Webb J. K., Yahil A., 1996, ApJ, 460, L85.
Ferrara A., Giallongo E., 1996, MNRAS, *in press*.
Fontana A., Ballester P., 1995, *ESO The Messenger*, 80, 37.
Giallongo E., Cristiani, S., D'Odorico S., Fontana A., Savaglio S., 1996, ApJ, *in press*.
Giallongo, E., Cristiani, S., Fontana, A., Trevese, D. 1993, ApJ, 416, 137.
Giallongo, E., D'Odorico, S., Fontana, A., McMahon, R. G., Savaglio, S., Cristiani, S., Molaro, P., Trevese, D. 1994, ApJL, 425, L1.
Giallongo E., Petitjean P., 1994, ApJ, 426, L61.
Haardt F., Madau P., 1996, ApJ, 461, 20.
Hernquist L., Katz N., Weinberg D. .H., Miralda–Escudé J., 1996, ApJ, 457, L51.
Hu E. M., Kim T.-S., Cowie L. L., Songaila A., Rauch M., 1995, AJ, 110, 1526.
Jakobsen P., Boksenberg A., Deharveng J. M., Greenfield P., Jedrzejewski R., Paresce F., 1994, Nat, 370, 35.
Lanzetta, K. M., Bowen, D. V., Tytler, D., Webb, J. K., 1995, ApJ, 442, 538.
Lu L., Sargent W. L. W., Barlow T. A., 1996, Contribution to "Cosmic Abundances", the proceedings of the 6th Annual October Astrophysical Conference in Maryland, *in press*.
Madau P., 1992, ApJ, 389, L1.
Miralda–Escudé J., Ostriker J. P., 1990, ApJ, 350, 1.
Miralda–Escudé J., Cen R., Ostriker J. P., Rauch M., 1996, ApJ, *submitted*.
Molaro, P., D'Odorico, S., Fontana, A., Savaglio, S., Vladilo, G., 1995, A&A, 308, 1.
Møller P., Jakobsen P., Perryman M. A. C., 1993, A&A, 287, 719.
Pei Y. C., 1995, ApJ, 438, 623.
Petitjean P., Bergeron J., 1994, A&A, 283, 759.
Petitjean P., Rauch M., Carswell R. F., 1994, A&A, 291, 29.
Rauch M., Carswell R. F., Webb J. K., Weymann R. J., 1993, MNRAS, 260, 589.
Savaglio S., D'Odorico S., Møller P., 1994, A&A, 281, 331.
Schneider, D. P., Schmidt, M., Gunn, J. E., 1989, AJ, 98, 1507.
Songaila A., Hu E. M., Cowie L. L., 1995, Nat, 375, 124.
Steidel C. C., Dickinson M., Persson S. E., 1994, ApJ, 437, L75.
Stone, R. P. S. 1977, Ap. J., 218, 767.
Stone, R. P. S., Baldwin, J. A. 1983, MNRAS, 204, 347.
Stone, R. P. S., Baldwin, J. A. 1984, MNRAS, 206, 241.
Timmes F. X., Woosley S. E., Weaver T. A., 1995, ApJS, 98, 617.
Tytler D., Fan X.-M., Burles S., Cottrell L., Davis C., Kirkman D., Zuo L., 1995, *Proceedings of the ESO Workshop on Quasars Absoon Lines*, ed. G. Meylan, p289.
Wheeler J. C., Sneden C., Truran J. W., 1989, ARA&A, Vol. 27, ed. G. Burbidge (Palo Alto: Annual Reviews), 279.
Walsh J. R., 1992, *HST and New Oke Spectrophotometric Standard Stars–Flux Tables and Finding Charts*.
Wampler E. J., Bergeron J., Petitjean P., 1993, A&A, 273, 15.
Webb J.K., Parnell H.C., Carswell R.F., McMahon R.G., Irwin M.J., Hazard C., Ferlet R., Vidal–Madjar A. 1988, The ESO Messenger, 51, 15.
Williger G. M., Baldwin J. A., Carswell R. F., Cooke A. J., Hazard C., Irwin M. J., McMahon R. G., Storrie–Lombardi L., 1994, ApJ, 428, 574.